Granger Causality Network Reconstruction of Conductance-Based Integrate-and-Fire Neuronal Systems

Douglas Zhou[1]*, Yanyang Xiao[1], Yaoyu Zhang[1], Zhiqin Xu[1], David Cai[1,2,3]*

1 Department of Mathematics, MOE-LSC, and Institute of Natural Sciences, Shanghai Jiao Tong University, Shanghai, China, **2** Courant Institute of Mathematical Sciences and Center for Neural Science, New York University, New York, New York, United States of America, **3** NYUAD Institute, New York University Abu Dhabi, Abu Dhabi, United Arab Emirates

Abstract

Reconstruction of anatomical connectivity from measured dynamical activities of coupled neurons is one of the fundamental issues in the understanding of structure-function relationship of neuronal circuitry. Many approaches have been developed to address this issue based on either electrical or metabolic data observed in experiment. The Granger causality (GC) analysis remains one of the major approaches to explore the dynamical causal connectivity among individual neurons or neuronal populations. However, it is yet to be clarified how such causal connectivity, i.e., the GC connectivity, can be mapped to the underlying anatomical connectivity in neuronal networks. We perform the GC analysis on the conductance-based integrate-and-fire (I&F) neuronal networks to obtain their causal connectivity. Through numerical experiments, we find that the underlying synaptic connectivity amongst individual neurons or subnetworks, can be successfully reconstructed by the GC connectivity constructed from voltage time series. Furthermore, this reconstruction is insensitive to dynamical regimes and can be achieved without perturbing systems and prior knowledge of neuronal model parameters. Surprisingly, the synaptic connectivity can even be reconstructed by merely knowing the raster of systems, i.e., spike timing of neurons. Using spike-triggered correlation techniques, we establish a direct mapping between the causal connectivity and the synaptic connectivity for the conductance-based I&F neuronal networks, and show the GC is quadratically related to the coupling strength. The theoretical approach we develop here may provide a framework for examining the validity of the GC analysis in other settings.

Citation: Zhou D, Xiao Y, Zhang Y, Xu Z, Cai D (2014) Granger Causality Network Reconstruction of Conductance-Based Integrate-and-Fire Neuronal Systems. PLoS ONE 9(2): e87636. doi:10.1371/journal.pone.0087636

Editor: Daniele Marinazzo, Universiteit Gent, Belgium

Received September 19, 2013; **Accepted** December 25, 2013; **Published** February 19, 2014

Copyright: © 2014 Zhou et al. This is an open-access article distributed under the terms of the Creative Commons Attribution License, which permits unrestricted use, distribution, and reproduction in any medium, provided the original author and source are credited.

Funding: D.Z. is supported by Shanghai Pujiang Program (Grant No. 10PJ1406300), National Science Foundation in China (Grant No. 11101275 and No. 91230202), and the Scientific Research Foundation for the Returned Overseas Chinese Scholars from State Education Ministry in China. D.C. is supported by NSF-DMS-1009575. All authors are also supported by a research grant G1301 from NYU Abu Dhabi Research Institute. Y.X., Y.Z., and Z.X. were partially supported by an Undergraduate Research Program in Zhiyuan College at Shanghai Jiao Tong University. The funders had no role in study design, data collection and analysis, decision to publish, or preparation of the manuscript.

Competing Interests: The authors have declared that no competing interests exist.

* E-mail: zdz@sjtu.edu.cn (DZ); cai@cims.nyu.edu DC)

Introduction

The relation between structure and function is one of the central research themes in biology. In order to fully understand the function of biological organisms, it is often important to analyze the structure of the systems [1–3]. The characterization of structure can be different with respect to the scales one is interested in. On the molecular level, the structure may refer to microscopic configurations of atoms, e.g., in hierarchical protein folding. Whereas, at the system level, such as neuronal circuitry, the structure often refers to the anatomical connections amongst neurons. To find the wiring diagram, i.e., synaptic connectivity, is often regarded as a key step towards understanding of the information processing and function of the brain [4–6]. New experimental observation tools, such as diffusion tensor imaging, are useful to tract fiber pathways in the whole brain, however, they usually have an insufficient spatial resolution and cannot be used to infer connections at the cellular level. Systematic assessment of global network synaptic connectivity through direct electrophysiological assays has remained technically infeasible, even for some simple systems such as dissociated neuronal culture [7–9]. However, it is relatively easy in experiment to obtain dynamical activities of neuronal populations or individual neurons through, e.g., local field potential, spike trains measurement, magnetoencephalography (MEG), electroencepholography (EEG), or functional magnetic resonance imaging (fMRI). Based on experimentally measured data, many network analysis approaches have been developed in attempt to probe the underlying brain connectivity through various statistical approaches [10–13], such as Granger causality [14–16] and dynamic Bayesian inference [17,18]. Through these analyses, the obtained connectivity is often referred to as functional or effective connectivity [19]. However, such functional (effective) connectivity obtained from different computational analysis is often different from one another [20,21]. Conceptually, they are also different from the structural (synaptic) connectivity. To infer the underlying network structure from observation, it is desirable to explore the relationship between structural and functional connectivity [22–25].

Understanding of how the functional connectivity is mapped to the anatomical synaptic connectivity in the brain remains one of the major challenges in systems neuroscience [26–29].

In this work, we study the relationship between structural connectivity and a particular functional connectivity which we will describe presently for conductance-based integrate-and-fire (I&F) neuronal networks. It has been shown in experiment that I&F models can statistically faithfully capture the response of cortical neurons under in-vivo-like currents in terms of both firing dynamics and subthreshold membrane dynamics [30–33]. In theoretical and computational neuroscience, the conductance-based I&F neuron has served as an efficient reduced model of cortical neurons to study their statistical spike-encoding properties [34,35]. For instance, the I&F neuron has been widely used as basic neuronal units for modeling large-scale cortical dynamics to investigate information processing in certain areas of the brain [36–42]. In our study, the structural connectivity of I&F networks denotes synaptic connections between neurons, which are characterized by the adjacency matrix of the network. The particular functional connectivity of I&F networks in our work denotes the connectivity constructed by the Granger causality (GC) analysis. The notion of GC was originally introduced by Wiener to determine causal influence from one dynamical variable $\mathbf{X}(t)$ to the other $\mathbf{Y}(t)$ [43]. It was further mathematically formulated using linear regression/prediction models [43–45]. In this framework, if the prediction of $\mathbf{Y}(t)$ can be improved by incorporating the information in the history of $\mathbf{X}(t)$, it is said that there exists a causal connection from the time series $\mathbf{X}(t)$ to $\mathbf{Y}(t)$. Due to its simplicity and easy implementation, the GC theory has been extensively applied to study the functional connectivity of networks in neuroscience as well as in other scientific fields such as systems biology, medical engineering, economics, and social science [14,46]. By using voltage or spike train time series obtained from the I&F network dynamics, the functional connectivity of I&F networks can be obtained from the GC analysis, which we will term as the GC connectivity, and describe this connectivity by the causal adjacency matrix.

The main theoretical issue we address in this work is whether we can establish a direct, quantitative mapping between the structural connectivity and the GC connectivity for I&F neuronal networks. That is, whether the underlying structural connectivity, which is usually not easy to assess in experiment, can be extracted by using the GC analysis. There are several challenges in this task: (i) the GC theory is based on linear regression models and assumes that the causal relationship can be well captured by low order statistics (up to the variance) of signals, e.g., Gaussian time series [47]. Theoretically, it has yet to determine whether the linear GC framework is applicable to I&F systems, whose dynamics are nonlinear and non-smooth; (ii) the notion of GC connectivity is statistical rather than structural, i.e., quantification of directed statistical correlation between dynamical elements, whereas the structural connectivity corresponds to physical connections between dynamical units. A priori, there is no obvious reason that these two types of connectivity are always identical to each other [9,21,48]. For instance, there were indications that strong effective connections could exist between regions with no direct structural connections [23,49,50] and the functional connectivity could vary under different dynamical states associated with the same structural network [3,51].

We first develop a reliable numerical algorithm for obtaining the GC connectivity of I&F networks. Through numerical studies, we show that the GC connectivity is highly coincident with the structural connectivity, i.e., the synaptic connectivity between neurons in a network can be well reconstructed by the causal connectivity obtained from the GC analysis on voltage time series. We point out that this reconstruction can be achieved despite the fact that the dynamics of I&F networks are both nonlinear and non-smooth. As demonstrated in our numerical results, this reconstruction is quite robust as long as the time series are reasonably long for the system to reach a statistically steady state. The reconstruction is also insensitive to the system size and is independent of dynamical regimes. We then investigate the theoretical underpinning of this network reconstruction by means of the spike-triggered correlation (STC) approach. Our analysis shows that the STC on voltage time series, often a standard method used for inference of connectivity in experiment [52,53], cannot capture the correct inference of the underlying synaptic connections between neurons. This failure has to do with the fact that voltage signals usually have a finite autocorrelation time. We further show that the STC on voltage-signal residuals, i.e., whitened signals obtained from regression models, is able to link the GC connectivity and the structural connectivity of the network. This is achieved by first establishing the structure of STC on residuals to reflect the underlying coupling between neurons, then showing this STC is linearly related to residual cross-correlations. Further, by solving the Yule-Walker equations with respect to residuals, we can obtain a relation between GC and the residual cross-correlations for the I&F networks, thus connecting GC to the underlying coupling between neurons through STC on residuals. In addition, we can obtain the relationship that GC for neuron j to neuron i is proportional to S^2, where S is the synaptic coupling strength from neuron j to neuron i.

To investigate the range of applicability of our method, we further demonstrate that the GC analysis is also capable of detecting synaptic connections between individual neurons and a subnetwork of neurons (i.e., a group of interacting neurons), or connections between subnetworks. This is motivated by the signals measured by extracellular recordings in experiment, i.e., the local field potential. Our results indicate that the synaptic connection may also be detected from measured signals between intracellular (individual neuron) and extracellular recordings (a group of neurons, i.e., subnetworks). In addition, we show that the network reconstruction through the GC theory can also be achieved using spike train time series. In comparison with the precise voltage-trace measurement, we note that spike train time series are relatively easy to measure in experiment, thus, rendering spike-train GC analysis particularly useful for practical settings. This is rather striking in that one can essentially reconstruct the synaptic connectivity of I&F networks by only examining the raster plot of a group of neurons. In addition, we also demonstrate that our reconstruction can be extended to networks with both excitatory and inhibitory neurons, or to more realistic neuronal networks, e.g., of the exponential I&F neurons. Note that our results provide a direct link between the GC connectivity and the structural connectivity with no intervention of systems and no prior knowledge of neuronal model parameters. Therefore, this method may be potentially useful in experiment to infer the structural information of neuronal networks. Because the GC theory is often used to investigate the direction of information flow within networks, our work may also shed light on how propagation of information flow within networks can be influenced by the network topology.

Results

The systems we study are conductance-based, integrate-and-fire type neuronal networks [See Eqs. (23), (24) and (25) in *Methods*]. As mentioned previously, with in-vivo-like current injection, the I&F

neuronal model can capture well both the firing rate and subthreshold dynamics of cortical neurons [30,31]. Consequently, networks of I&F neurons have served as prototypical theoretical models to provide insight into fascinating dynamics of many neuronal networks in the brain [32,33,35,54].

The Granger causality characterizes causal interactions between time series by distinguishing the driver from the recipient (See theoretical definitions in *Methods*), namely, the driver, which is earlier than the recipient, contains information about the future of the recipient, and thus the variance of the prediction error is reduced when the information of the driver is incorporated. In general, the causal influence between time series reflects a drive-response scenario and this influence can be either reciprocal or unidirectional. As discussed later, such causality which is based on temporality is characterized by the directional correlation relations between time series.

We apply the Granger causality analysis to these widely used I&F neuronal networks to investigate the relationship between causal and structural connectivities (See GC algorithm in *Methods*). By applying the GC algorithm to the I&F networks, we can obtain all the GC values from neuron j to neuron i, denoted by $F_{V_j \to V_i}$, for $i,j=1,2,\cdots,N$. Then, we perform the p-value test ($p=0.001$ in our simulations) to determine a GC threshold F_{T} (See Text S1 for more details). If $F_{V_j \to V_i} > F_{\mathrm{T}}$, we define that there is a significant causal interaction from the jth neuron to the ith neuron and denote this by $G_{ij}=1$. Otherwise, we say there is no causal influence from the jth neuron to the ith neuron and denote this by $G_{ij}=0$. Because GC interactions between two neurons are in general not symmetric, by representing them as edges in a graph, we can define a directed graph or a causal connectivity network, as characterized by the matrix $\boldsymbol{G}=(G_{ij})$, for the I&F systems [55,56]. Meanwhile, the structural connectivity of our I&F system is characterized by the synaptic adjacency matrix, denoted by $\boldsymbol{A}=(A_{ij})$ (See *Methods*). Note that, the causal connectivity can be viewed as a type of functional connectivity [19,29], whereas the structural connectivity reflects physical connectivity. As discussed in the *Introduction*, our causal connectivity is a statistical measure, and it is, in general, not equivalent to the underlying physical connections between dynamical variables [56].

Causal connectivity vs. structural connectivity for I&F networks

As described above, the GC connectivity can be characterized by the causal adjacency matrix $\boldsymbol{G}=(G_{ij})$, whereas the structural connectivity is characterized by the synaptic adjacency matrix $\boldsymbol{A}=(A_{ij})$, $i,j=1,2,\cdots,N$. In the following, we discuss the relationship between $\boldsymbol{G}$ and $\boldsymbol{A}$ for the I&F networks, i.e., the relationship between GC connectivity and structural connectivity.

Figure 1A and C shows examples of synaptic connectivity (A_{ij}) between neurons for a two-neuron and a three-neuron networks. Figure 1B and D displays the corresponding causal adjacency matrix (G_{ij}) constructed by using our GC algorithm on the voltage time series. It can be clearly seen that the causal connectivity is coincident with the synaptic connectivity. These examples present compelling evidence that the synaptic adjacency matrix of the I&F networks can be successfully reconstructed by using the GC algorithm on neurons' voltage trajectories.

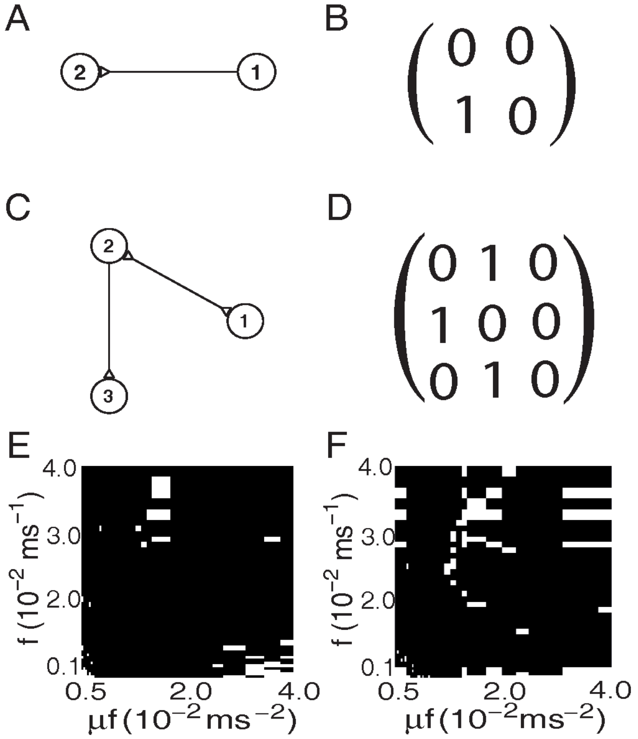

Figure 1. GC connectivity for small excitatory networks. For networks of two excitatory neurons and three excitatory neurons in (A) and (C), the edge with only a triangle at the end signifies a directed connectivity. Parameters in (A)-(D) are chosen as $\mu=1\ \mathrm{ms}^{-1}$ (Poisson input rate), $f=0.007\ \mathrm{ms}^{-1}$ (Poisson input strength), and the coupling strength $S=0.01\ \mathrm{ms}^{-1}$ (the corresponding EPSP is ~ 1 mV). (A) A two-neuron network with only a synaptic connection from neuron 1 to neuron 2. (B) Causal adjacency matrix $\boldsymbol{G}=(G_{ij})$ constructed by GC, which captures the synaptic connectivity in (A). (C) A three-neuron network with a synaptic connection from neuron 2 to neuron 3 and with bidirectional synaptic connections between neuron 1 and neuron 2. (D) Causal adjacency matrix $\boldsymbol{G}=(G_{ij})$ constructed by GC, which captures the synaptic connectivity in (C). The coincidence between the synaptic adjacency matrix $\boldsymbol{A}$ and the causal adjacency matrix $\boldsymbol{G}$ as a function of rate μ and magnitude f in the Poisson drive for (E) the two-neuron network as shown in (A), and (F) the three-neuron network as shown in (C). The parameter region labeled by the white color indicates that $\boldsymbol{A} \neq \boldsymbol{G}$, and by the black color indicating that $\boldsymbol{A}=\boldsymbol{G}$.
doi:10.1371/journal.pone.0087636.g001

Next, we address the question of whether these successful reconstructions are merely accidental cases or whether there is a large class of networks that are amenable to this analysis. To examine whether the reconstruction is dependent on particular dynamical regimes, which are often described by a particular choice of network system parameters, we investigate the robustness of the reconstruction by scanning the magnitude f and the rate μ in the Poisson drive of the I&F networks [See Eq. (23) in *Methods*]. The choice of these parameters covers the realistic firing rates ($5\sim150$ Hz) of real neurons [35,57]. Note that there are typically three dynamical regimes for the I&F neurons for each fixed input strength f: (i) a highly fluctuating regime when the input rate μ is low; (ii) an intermediate regime when μ is moderately high; (iii) a low fluctuating or mean driven regime when μ is very high [58,59]. Figure 2A–C shows the voltage trajectories of two neurons for different choices of input rate μ with the input strength f fixed. It can be seen from Fig. 2A–C that the firing pattern is rather irregular when μ is low ($\sim 0.3\mathrm{ms}^{-1}$), whereas the spiking activity of neurons becomes relatively regular (nearly periodic) when μ is very high ($\sim 2.0\mathrm{ms}^{-1}$). For all these dynamical regimes, we can demonstrate that there is a wide range of the network parameters whose synaptic connectivity can be analyzed using the GC analysis. As shown in Fig. 1E and F, the GC connectivity ($\boldsymbol{G}$) and the synaptic connectivity ($\boldsymbol{A}$) are highly coincident with each other

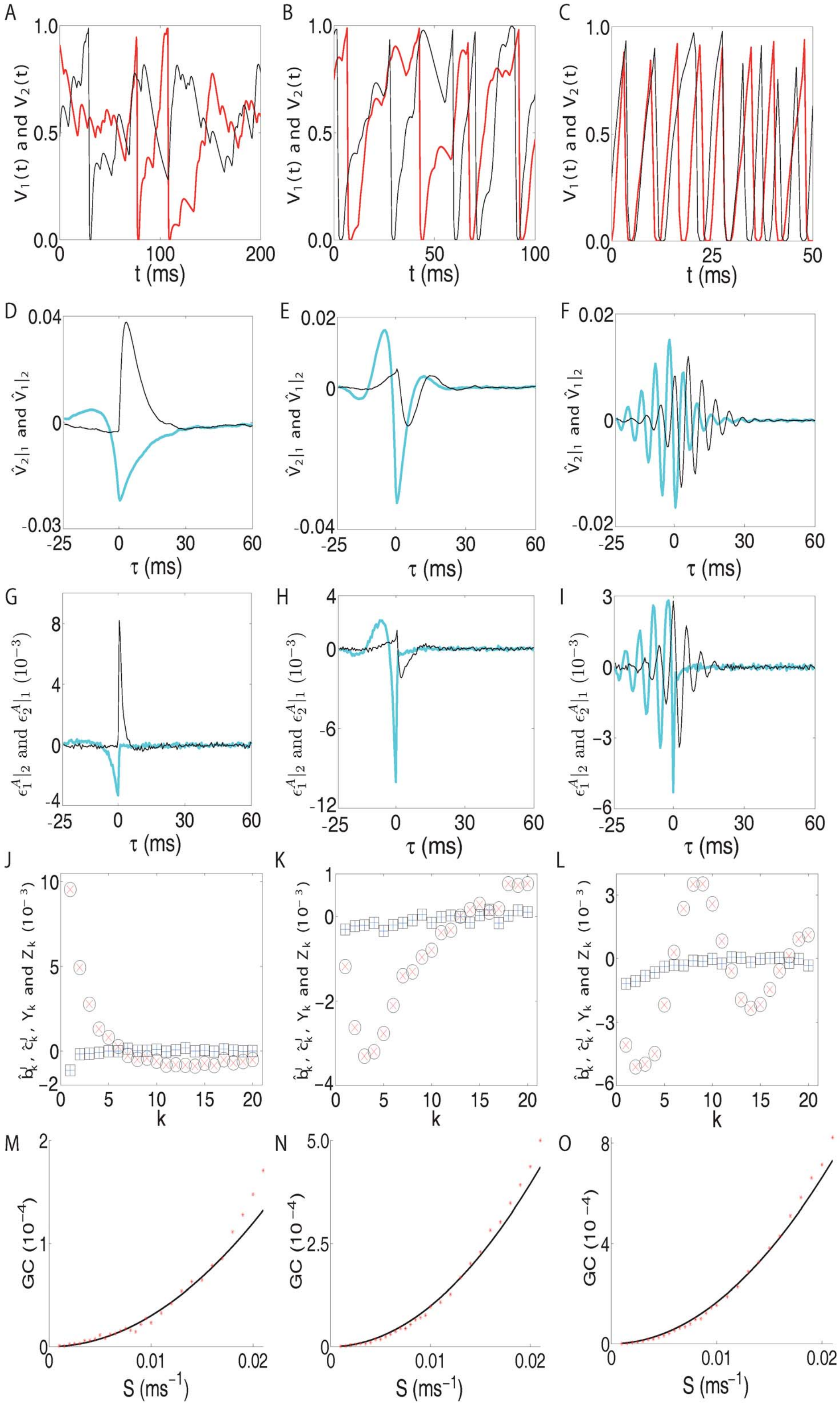

Figure 2. Characteristics of different dynamical regimes. Illustrated here are the dynamic characteristics of the two-excitatory-neuron network in Fig. 1A with different Poisson input rate μ for highly fluctuating regime [(A),(D),(G),(J) and (M)] with $\mu \sim 0.3\mathrm{ms}^{-1}$, intermediate regime [(B),(E),(H),(K) and (N)] with $\mu \sim 0.8\mathrm{ms}^{-1}$ and mean-driven regime [(C),(F),(I),(L) and (O)] with $\mu \sim 2.0\mathrm{ms}^{-1}$. The fixed input strength $f \sim 0.02\ \mathrm{ms}^{-1}$. For these three dynamical regimes, we plot the corresponding quantities: (A), (B), and (C) are voltage trajectories $V_1(t)$ (black online) and $V_2(t)$ (red online). (D), (E), and (F) are spike-triggered correlation on voltage [Eq. (1)]: $\hat{V}_1|_2(\tau)$ (cyan online) and $\hat{V}_2|_1(\tau)$ (black online). (G), (H), and (I) are spike-triggered correlation on residuals [Eq. (2)]: $\epsilon_1^{\mathrm{A}}|_2(\tau)$ (cyan online) and $\epsilon_2^{\mathrm{A}}|_1(\tau)$ (black online). (J), (K), and (L) are numerically computed regression coefficients $\hat{b}_k^{\mathrm{J}}$

(blue "plus" online), $\hat{c}_k^{\mathrm{J}}$ (red "cross" online) and their corresponding approximations $Y_k = r_k/\mathrm{Var}(\epsilon_2^{\mathrm{A}})$ ("square" symbol), $Z_k = r_{-k}/\mathrm{Var}(\epsilon_1^{\mathrm{A}})$ ("circle" symbol). (M), (N), and (O) are the GC $F_{V_1 \to V_2}$ (red "star" online) as a function of coupling strength S, the line (black online) is a quadratic fit.
doi:10.1371/journal.pone.0087636.g002

for both two-neuron and three-neuron networks over a wide range of dynamical regimes.

We further examine whether the synaptic connectivity of large networks with multiple neurons can be revealed by the GC connectivity analysis. For a network of 100 neurons with random connectivity, its synaptic adjacency matrix (A_{ij}) is shown in Fig. 3A, where the total number of nonzero A_{ij}, as indicated by the black color, is approximately 2000. Applying the GC analysis to this network, we can construct its causal connectivity matrix (G_{ij}). Figure 3B shows the difference between $\boldsymbol{A}$ and $\boldsymbol{G}$, where the white color represents $|A_{ij} - G_{ij}| = 1$, i.e., $A_{ij} \neq G_{ij}$, and the black color represents $A_{ij} = G_{ij}$. It can be seen that the synaptic adjacency matrix $\boldsymbol{A}$ can be successfully reconstructed by the causal adjacency matrix $\boldsymbol{G}$ with very high accuracy ($\geq 98\%$). Incidentally, we also point out an interesting phenomenon as observed for the GC connectivity of large excitatory neuronal networks: if we rank the GC by magnitude for all possible directed connections between neurons, there often is a gap separating these ranked GC values as indicated by the gray horizontal line (blue online) in Fig. 3C. This gap clearly divides the GC values into two distinct groups. Surprisingly, by using this gap, for example, by choosing a horizontal line within the gap as the GC threshold F_{T}, we obtain that $\boldsymbol{G}$ is identical to $\boldsymbol{A}$.

Mechanism underlying the successful reconstruction

In this section, we address the issue of why the GC framework, based on linear systems, can be used to reveal the synaptic connectivity of nonlinear network dynamics of I&F neurons. For dynamical systems of pulse-coupled type, such as I&F neurons, the spike-triggered correlation (STC) or spike-triggered averaging method has been widely applied in studies of synaptic connections in such systems [52,60]. The STC on voltages from the jth neuron to the ith neuron is defined as

$$\hat{V}_i|_j(\tau) = \langle \hat{V}_i(T_{j,k} + \tau) \rangle_k, \tag{1}$$

where $\hat{V}_i(t) = V_i(t) - \mathbb{E}[V_i(t)]$ has zero mean, $T_{j,k}$ is the kth spike time of the jth neuron as defined in Eq. (23) (See *Methods*) and $\langle \cdot \rangle_k$ is the average with respect to k, i.e., average over all spikes of the jth neuron. Note that, the STC contains the information of both the statistics of the spike drive from the jth neuron and the response of the ith neuron [52,60]. Therefore, this drive-response scenario apparently reflects the causal connectivity from the jth neuron to the ith neuron. On the other hand, the existence of this drive-response relation might imply the existence of synaptic connectivity from the jth neuron to the ith neuron, i.e., $A_{ij} = 1$. Therefore, it appears that the feature of STC on voltage can be used to relate the causal connectivity to the synaptic connectivity for the I&F network system.

For the two-neuron network in Fig. 1A, the STCs on voltages between neuron 1 and neuron 2 $[\hat{V}_1|_2(\tau)$ and $\hat{V}_2|_1(\tau)]$ in the three different dynamical regimes are displayed in Fig. 2D–F. From the definition of STC [Eq. (1)], if the ith neuron's response $\hat{V}_i(T_{j,k} + \tau)$, averaged over all the spikes of the jth neuron, exhibits significant deviations from zero when $\tau > 0$, it might imply that the jth neuron is presynaptic to the ith neuron, otherwise $\langle \hat{V}_i(T_{j,k} + \tau) \rangle_k$ should be nearly zero after statistical average [52,60,61]. However, as shown in Fig. 2D–F, both STCs, $\hat{V}_1|_2(\tau)$ and $\hat{V}_2|_1(\tau)$, exhibit significant deviations from zero for $\tau > 0$ when τ is small and naturally vanish when τ is sufficiently large in all dynamical regimes shown in Fig. 2A–C. These nonzero features in STCs, $\hat{V}_1|_2(\tau)$ and $\hat{V}_2|_1(\tau)$, may suggest that the connections between two neurons are bidirectional [61,62]. However, from the network synaptic connectivity as shown in Fig. 1A, there is only a unidirectional synaptic connection from neuron 1 to neuron 2. Therefore, one needs to address the question of why the STC $\hat{V}_1|_2(\tau)$, similarly $\hat{V}_2|_1(\tau)$, exhibit nonzero features for $\tau > 0$ despite the fact that there is no synaptic connection from neuron 2 to neuron 1. Intuitively, we can understand the phenomenon as follows: because the voltage signal $\hat{V}_1(t)$ is not white, i.e., there is a finite correlation time for the voltage signal, the future of $\hat{V}_1$ will be correlated with its own history. On the other hand, neuron 1 is presynaptic to the neuron 2, thus giving rise to the possibility that $\hat{V}_2(t)$ is also correlated with the history of $\hat{V}_1$. Therefore, $\hat{V}_2(t)$ would be likely correlated with the future of $\hat{V}_1$. This correlation is reflected in the nonzero feature of the STC $\hat{V}_1|_2(\tau)$ for $\tau > 0$, and it can give rise to an incorrect inference of the synaptic connection from neuron 2 to neuron 1.

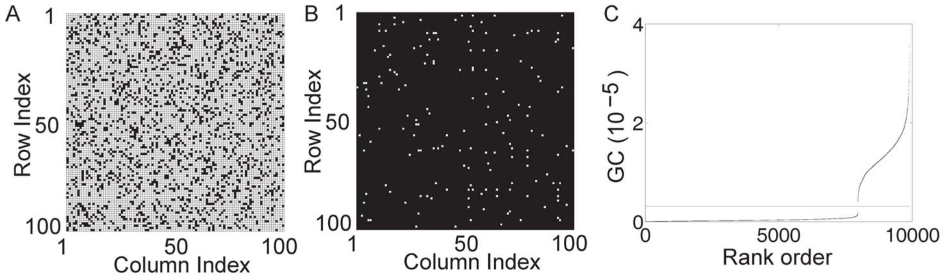

Figure 3. GC connectivity for large excitatory networks. For an I&F network of 100 excitatory neurons with random connectivity, the synaptic adjacency matrix $\boldsymbol{A} = (A_{ij})$ is shown in (A) with the white color indicating that $A_{ij} = 0$ and the black color for $A_{ij} = 1$. The total number of nonzero A_{ij} is ~ 2000 (the percentage of connections is $\sim 20\%$) and the average neuronal firing rate is ~ 20Hz. (B) The absolute difference between $\boldsymbol{A}$ and the causal adjacency matrix $\boldsymbol{G}$, i.e., $|A_{ij} - G_{ij}|$. The white color indicates that $|A_{ij} - G_{ij}| = 1$, i.e., $A_{ij} \neq G_{ij}$ and the black color when $A_{ij} = G_{ij}$. By significance test ($p = 0.001$, See Text S1 for more details), the total number of $A_{ij} \neq G_{ij}$ is 163 out of $\sim 10{,}000$ possible pairs of connections. (C) Ranked GC in order of magnitude with the horizontal line (blue online) indicating a threshold in the gap of the ranked GC. Parameters are chosen as $\mu = 0.24\ \mathrm{ms}^{-1}$ (Poisson input rate), $f = 0.02\ \mathrm{ms}^{-1}$ (Poisson input strength), and the coupling strength $S = 0.005\ \mathrm{ms}^{-1}$ (the corresponding EPSP is ~ 0.5 mV).
doi:10.1371/journal.pone.0087636.g003

From the above argument, the nonzero feature of the STC $\hat{V}_1|_2(\tau)$ is closely related to the finite-time autocorrelation structure of voltage signals. This has led us to investigate the STC on signals without finite-time autocorrelations, i.e., whitened signals, in order to extract correct synaptic connectivity between neurons. Note that, the residuals $\epsilon_1^{\mathrm{A}}(t)$ and $\epsilon_2^{\mathrm{A}}(t)$, as obtained in auto regression (AR) models [See Eq. (17) in *Methods*], are whitened signals [44,45], i.e., with only instantaneous correlation. Therefore, we may study the STC on residuals ϵ_i^{A} and ϵ_j^{A}:

$$\epsilon_i^{\mathrm{A}}|_j(\tau) = \langle \epsilon_i^{\mathrm{A}}(T_{j,k}+\tau)\rangle_k. \tag{2}$$

As shown in Fig. 2G–I, for $\tau > 0$, the STC $\epsilon_2^{\mathrm{A}}|_1(\tau)$ possesses similar features to that of the STC $\hat{V}_2|_1(\tau)$, indicating the existence of synaptic connectivity from neuron 1 to neuron 2. However, unlike the STC $\hat{V}_1|_2(\tau)$, the STC $\epsilon_1^{\mathrm{A}}|_2(\tau)$ statistically vanishes for $\tau > 0$, suggesting that neuron 2 is not presynaptic to neuron 1. These results indicate that the STC on residuals, i.e., whitened signals, can provide a correct inference about the unidirectional connection between the two neurons.

As the STC on residuals may be used to successfully detect the synaptic connectivity between neurons, it is natural to ask whether the GC connectivity between the signals of residuals are related to the underlying mechanism for the success of the reconstruction of networks. From the AR models for $\hat{V}_1(t)$ and $\hat{V}_2(t)$ [See Eq. (17) in *Methods*], we can construct the moving average representations of $\hat{V}_1(t)$, $\hat{V}_2(t)$ in terms of residuals $\epsilon_1^{\mathrm{A}}(t)$, $\epsilon_2^{\mathrm{A}}(t)$ [63,64].

$$\begin{aligned}\hat{V}_1(t) &= \sum_{k>0} P_k \epsilon_1^{\mathrm{A}}(t-k) + \epsilon_1^{\mathrm{A}}(t),\\ \hat{V}_2(t) &= \sum_{k>0} Q_k \epsilon_2^{\mathrm{A}}(t-k) + \epsilon_2^{\mathrm{A}}(t),\end{aligned} \tag{3}$$

where P_k and Q_k are constant coefficients. Then, substituting Eq. (3) into the joint regression (JR) models for $\hat{V}_1(t)$ and $\hat{V}_2(t)$ [See Eq. (18) in *Methods*], we obtain the corresponding JR models for $\epsilon_1^{\mathrm{A}}(t)$ and $\epsilon_2^{\mathrm{A}}(t)$:

$$\epsilon_1^{\mathrm{A}}(t) = \sum_{k>0} \hat{a}_k^{\mathrm{J}} \epsilon_1^{\mathrm{A}}(t-k) + \sum_{k>0} \hat{b}_k^{\mathrm{J}} \epsilon_2^{\mathrm{A}}(t-k) + \epsilon_{1,2}^{\mathrm{J}}(t), \tag{4a}$$

$$\epsilon_2^{\mathrm{A}}(t) = \sum_{k>0} \hat{c}_k^{\mathrm{J}} \epsilon_1^{\mathrm{A}}(t-k) + \sum_{k>0} \hat{d}_k^{\mathrm{J}} \epsilon_2^{\mathrm{A}}(t-k) + \epsilon_{2,1}^{\mathrm{J}}(t), \tag{4b}$$

where $\epsilon_{1,2}^{\mathrm{J}}(t)$ and $\epsilon_{2,1}^{\mathrm{J}}(t)$ are the same residuals as those in the original JR models for $\hat{V}_1(t)$ and $\hat{V}_2(t)$ [See Eq. (18) in *Methods*]. Note that Eqs. (4a) and (4b) can also be obtained by using the least-squares method. On the other hand, we can construct the AR models for $\epsilon_1^{\mathrm{A}}(t)$ and $\epsilon_2^{\mathrm{A}}(t)$ as

$$\begin{aligned}\epsilon_1^{\mathrm{A}}(t) &= \sum_{k>0} \hat{a}_k^{\mathrm{A}} \epsilon_1^{\mathrm{A}}(t-k) + \tilde{\epsilon}_1^{\mathrm{A}}(t),\\ \epsilon_2^{\mathrm{A}}(t) &= \sum_{k>0} \hat{d}_k^{\mathrm{A}} \epsilon_2^{\mathrm{A}}(t-k) + \tilde{\epsilon}_2^{\mathrm{A}}(t),\end{aligned} \tag{5}$$

Eqs. (4) and (5) represent JR and AR processes for residuals $\epsilon_1^{\mathrm{A}}(t)$ and $\epsilon_2^{\mathrm{A}}(t)$, respectively. By the definition of GC, we can obtain $F_{\epsilon_2^{\mathrm{A}}\to\epsilon_1^{\mathrm{A}}} = \ln\frac{\mathrm{Var}(\tilde{\epsilon}_1^{\mathrm{A}})}{\mathrm{Var}(\epsilon_{1,2}^{\mathrm{J}})}$ and $F_{\epsilon_1^{\mathrm{A}}\to\epsilon_2^{\mathrm{A}}} = \ln\frac{\mathrm{Var}(\tilde{\epsilon}_2^{\mathrm{A}})}{\mathrm{Var}(\epsilon_{2,1}^{\mathrm{J}})}$. Note that the residuals $\epsilon_1^{\mathrm{A}}(t)$ and $\epsilon_2^{\mathrm{A}}(t)$ are whitened signals. Therefore, the coefficients $\hat{a}_k^{\mathrm{A}}$, $\hat{d}_k^{\mathrm{A}}$ in the AR models (5) are zero and we have $\tilde{\epsilon}_1^{\mathrm{A}}(t) = \epsilon_1^{\mathrm{A}}(t)$, $\tilde{\epsilon}_2^{\mathrm{A}}(t) = \epsilon_2^{\mathrm{A}}(t)$. This yields that the GC is invariant as

$$F_{V_2\to V_1} = F_{\epsilon_2^{\mathrm{A}}\to\epsilon_1^{\mathrm{A}}} \quad \text{and} \quad F_{V_1\to V_2} = F_{\epsilon_1^{\mathrm{A}}\to\epsilon_2^{\mathrm{A}}}. \tag{6}$$

From Eq. (6), it can be seen that the causal connectivity is indeed embedded in the whitened residuals $\epsilon_1^{\mathrm{A}}(t)$ and $\epsilon_2^{\mathrm{A}}(t)$. In the following, we will show how the STC on residuals bridges the causal connectivity and the synaptic connectivity.

We first derive analytical expressions of GC for the I&F networks and show that they are closely related to the residual cross-correlation between ϵ_1^{A} and ϵ_2^{A}. Multiplying Eq. (4a) by the residual $\epsilon_1^{\mathrm{A}}(t-l)$ or $\epsilon_2^{\mathrm{A}}(t-l)$, for $l=1,\ 2,\ \cdots$, and taking expectations, we obtain the Yule-Walker equations [63,64] with respect to the coefficients $\hat{a}_k^{\mathrm{J}}$ and $\hat{b}_k^{\mathrm{J}}$ as

$$\begin{aligned}\mathrm{Var}(\epsilon_1^{\mathrm{A}})\hat{\boldsymbol{a}}^{\mathrm{J}} + \boldsymbol{R}\hat{\boldsymbol{b}}^{\mathrm{J}} &= 0,\\ \boldsymbol{R}^{\mathrm{T}}\hat{\boldsymbol{a}}^{\mathrm{J}} + \mathrm{Var}(\epsilon_2^{\mathrm{A}})\hat{\boldsymbol{b}}^{\mathrm{J}} &= \boldsymbol{r}_+,\end{aligned} \tag{7}$$

where $\boldsymbol{R} = [r_{ij}]$ is the covariance matrix with $r_{ij} = \mathbb{E}[\epsilon_1^{\mathrm{A}}(t)\epsilon_2^{\mathrm{A}}(t+i-j)]$. The column vectors $\hat{\boldsymbol{a}}^{\mathrm{J}} = (\hat{a}_k^{\mathrm{J}})$, $\hat{\boldsymbol{b}}^{\mathrm{J}} = (\hat{b}_k^{\mathrm{J}})$ and $\boldsymbol{r}_+ = (r_k)$, for $k=1,\ 2,\cdots$, where $\hat{a}_k^{\mathrm{J}}$, $\hat{b}_k^{\mathrm{J}}$ and $r_k = \mathbb{E}[\epsilon_1^{\mathrm{A}}(t)\epsilon_2^{\mathrm{A}}(t-k)]$ are the kth component in the vectors. Similarly, if we multiply Eq. (4b) by the residual $\epsilon_1^{\mathrm{A}}(t-l)$ or $\epsilon_2^{\mathrm{A}}(t-l)$, for $l=1,\ 2,\ \cdots$, and take expectations, then we can obtain the Yule-Walker equations with respect to coefficients $\hat{c}_k^{\mathrm{J}}$ and $\hat{d}_k^{\mathrm{J}}$

$$\begin{aligned}\mathrm{Var}(\epsilon_1^{\mathrm{A}})\hat{\boldsymbol{c}}^{\mathrm{J}} + \boldsymbol{R}\hat{\boldsymbol{d}}^{\mathrm{J}} &= \boldsymbol{r}_-,\\ \boldsymbol{R}^{\mathrm{T}}\hat{\boldsymbol{c}}^{\mathrm{J}} + \mathrm{Var}(\epsilon_2^{\mathrm{A}})\hat{\boldsymbol{d}}^{\mathrm{J}} &= 0,\end{aligned} \tag{8}$$

where the column vectors $\hat{\boldsymbol{c}}^{\mathrm{J}} = (\hat{c}_k^{\mathrm{J}})$, $\hat{\boldsymbol{d}}^{\mathrm{J}} = (\hat{d}_k^{\mathrm{J}})$ and $\boldsymbol{r}_- = (r_{-k})$, for $k=1,\ 2,\cdots$, where $\hat{c}_k^{\mathrm{J}}$, $\hat{d}_k^{\mathrm{J}}$ and $r_{-k} = \mathbb{E}[\epsilon_1^{\mathrm{A}}(t)\epsilon_2^{\mathrm{A}}(t+k)]$ are the kth component in the vectors. Solving Eqs. (7) and (8), we obtain the regression coefficients as

$$\begin{aligned}&\hat{\boldsymbol{a}}^{\mathrm{J}} = -\boldsymbol{RKr}_+, \qquad \hat{\boldsymbol{b}}^{\mathrm{J}} = \mathrm{Var}(\epsilon_1^{\mathrm{A}})\boldsymbol{Kr}_+,\\ &\hat{\boldsymbol{c}}^{\mathrm{J}} = \mathrm{Var}(\epsilon_2^{\mathrm{A}})\boldsymbol{Hr}_-, \quad \text{and} \quad \hat{\boldsymbol{d}}^{\mathrm{J}} = -R^{\mathrm{T}}\boldsymbol{Hr}_-,\end{aligned} \tag{9}$$

where the matrices $\boldsymbol{K}$ and $\boldsymbol{H}$ are defined as $\boldsymbol{K} = [\mathrm{Var}(\epsilon_1^{\mathrm{A}})\mathrm{Var}(\epsilon_2^{\mathrm{A}})\boldsymbol{I} - \boldsymbol{R}^{\mathrm{T}}\boldsymbol{R}]^{-1}$ and $\boldsymbol{H} = [\mathrm{Var}(\epsilon_1^{\mathrm{A}})\mathrm{Var}(\epsilon_2^{\mathrm{A}})\boldsymbol{I} - \boldsymbol{RR}^{\mathrm{T}}]^{-1}$ with $\boldsymbol{I}$ being the identity matrix.

As mentioned previously, Eqs. (4) can also be obtained by using the least-squares method. From this viewpoint, by multiplying Eq. (4a) by $\epsilon_1^{\mathrm{A}}(t)$ and Eq. (5) by $\epsilon_2^{\mathrm{A}}(t)$, then taking expectations, we can obtain

$$\begin{aligned}\mathrm{Var}(\epsilon_1^{\mathrm{A}}) &= \boldsymbol{r}_+^{\mathrm{T}}\hat{\boldsymbol{b}}^{\mathrm{J}} + \mathrm{Var}(\epsilon_{1,2}^{\mathrm{J}}),\\ \mathrm{Var}(\epsilon_2^{\mathrm{A}}) &= \boldsymbol{r}_-^{\mathrm{T}}\hat{\boldsymbol{c}}^{\mathrm{J}} + \mathrm{Var}(\epsilon_{2,1}^{\mathrm{J}}).\end{aligned} \tag{10}$$

Substituting Eqs. (9) into Eqs. (10) and using the GC definition [See Eqs. (19) in *Methods*], we arrive at

$$\begin{aligned} F_{V_2\to V_1} &= -\ln\left(1-\boldsymbol{r}_+^{\mathrm{T}}\boldsymbol{K}\boldsymbol{r}_+\right) \quad \text{and} \\ F_{V_1\to V_2} &= -\ln\left(1-\boldsymbol{r}_-^{\mathrm{T}}\boldsymbol{H}\boldsymbol{r}_-\right). \end{aligned} \tag{11}$$

For small residual cross-correlation between ϵ_1^{A} and ϵ_2^{A}, which is consistent with our numerical simulation results for the I&F networks, namely, $r_i r_j \ll \mathrm{Var}(\epsilon_1^{\mathrm{A}})\mathrm{Var}(\epsilon_2^{\mathrm{A}})$ with i, j chosen as any integers, the matrices $\boldsymbol{K}$ and $\boldsymbol{H}$ can both be approximated by $\boldsymbol{I}/\mathrm{Var}(\epsilon_1^{\mathrm{A}})\mathrm{Var}(\epsilon_2^{\mathrm{A}})$. Therefore, the regression coefficients $\hat{b}_k^{\mathrm{J}}$ and $\hat{c}_k^{\mathrm{J}}$ in Eqs. (9) can be approximated by

$$\hat{b}_k^{\mathrm{J}} \approx \frac{r_k}{\mathrm{Var}(\epsilon_2^{\mathrm{A}})} \quad \text{and} \quad \hat{c}_k^{\mathrm{J}} \approx \frac{r_{-k}}{\mathrm{Var}(\epsilon_1^{\mathrm{A}})}. \tag{12}$$

As verified numerically in Fig. 2J–L, Eqs. (12) provide very good approximations of the regression coefficients $\hat{b}_k^{\mathrm{J}}$ and $\hat{c}_k^{\mathrm{J}}$ for the I&F networks. We observe that $\hat{b}_k^{\mathrm{J}} \approx 0$ and $\hat{c}_k^{\mathrm{J}} \neq 0$ as shown in Fig. 2J–L. From the GC theory [43–45], a vanishing $\hat{b}_k^{\mathrm{J}}$ indicates there is no causal influence from neuron 2 to neuron 1, whereas a nonvanishing $\hat{c}_k^{\mathrm{J}}$ indicates there is a causal influence from neuron 1 to neuron 2. This causal connectivity is consistent with the underlying synaptic connectivity. By definition, the residual cross-correlation r_k reflects the correlation between the future of neuron 1 [as embedded in $\epsilon_1^{\mathrm{A}}(t)$] and the history of neuron 2 [as embedded in $\epsilon_2^{\mathrm{A}}(t-k)$], whereas r_{-k} reflects the correlation between the future of neuron 2 and the history of neuron 1. Therefore, r_k and r_{-k} characterize the drive-response relationship between two neurons, as also captured by the regression coefficients $\hat{b}_k^{\mathrm{J}}$ and $\hat{c}_k^{\mathrm{J}}$ in JR models through Eqs. (12). Furthermore, the GC between two neurons [Eq. (11)] can be approximated by

$$F_{V_2\to V_1} \approx \frac{\boldsymbol{r}_+^{\mathrm{T}}\boldsymbol{r}_+}{\mathrm{Var}(\epsilon_1^{\mathrm{A}})\mathrm{Var}(\epsilon_2^{\mathrm{A}})} \quad \text{and} \quad F_{V_1\to V_2} \approx \frac{\boldsymbol{r}_-^{\mathrm{T}}\boldsymbol{r}_-}{\mathrm{Var}(\epsilon_1^{\mathrm{A}})\mathrm{Var}(\epsilon_2^{\mathrm{A}})}, \tag{13}$$

which provide a relation between the GC and the residual cross-correlations.

Next, we establish the relationship between the STC on residuals and their cross-correlations. Due to the firing-reset dynamics of I&F neurons, the magnitude of ϵ_1^{A} (ϵ_2^{A}) at each kth spike time $T_{1,k}$ ($T_{2,k}$) is much larger in absolute value than that at other times as can be seen from Fig. 4. Therefore, the residuals $\epsilon_1^{\mathrm{A}}(t)$ and $\epsilon_2^{\mathrm{A}}(t)$ can be approximated in the form of the Dirac delta functions as $\epsilon_i^{\mathrm{A}}(t) \approx -h_i \sum_k \delta(t-T_{i,k})$, $i=1,2$, where h_1 and h_2 are normalizing factors. Under this approximation, the STC on residuals [Eq. (2)] can be expressed as

$$\epsilon_1^{\mathrm{A}}|_2(\tau) \approx -\frac{r_\tau}{h_2 v_2} \quad \text{and} \quad \epsilon_2^{\mathrm{A}}|_1(\tau) \approx -\frac{r_{-\tau}}{h_1 v_1}, \tag{14}$$

where v_1 and v_2 are the firing rate of neuron 1 and neuron 2, respectively. From Eqs. (13) and (14), it can be seen that the GC $F_{V_1\to V_2} \neq 0$ is equivalent to the STC on residual $\epsilon_2^{\mathrm{A}}|_1(\tau) \neq 0$, and $F_{V_2\to V_1} = 0$ is equivalent to the STC on residual $\epsilon_1^{\mathrm{A}}|_2(\tau) = 0$ for $\tau > 0$. Therefore, the causal connectivity can be well extracted by the nonzero feature of STC on residuals. Note that, as discussed previously, the nonzero feature of STC on residuals is related to the pre-post synaptic connectivity between neurons as shown in Fig. 2G–I. Therefore, we can conclude that the causal connectivity captures well the synaptic connectivity for the I&F networks.

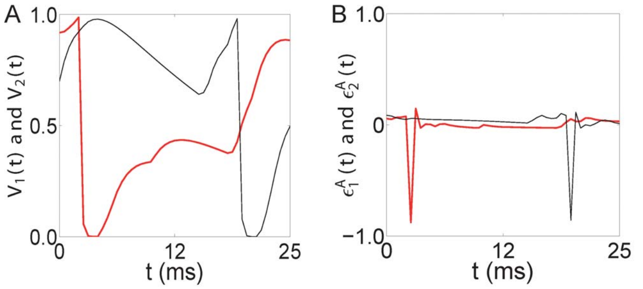

Figure 4. Trajectories of voltages and residuals. For the two-excitatory-neuron network in Fig. 1A, illustrated here are the sample trajectories of voltages in (A) $V_1(t)$ (black online) and $V_2(t)$ (red online), and corresponding trajectories of residuals in (B) $\epsilon_1^{\mathrm{A}}(t)$ (black online) and $\epsilon_2^{\mathrm{A}}(t)$ (red online).
doi:10.1371/journal.pone.0087636.g004

Finally, we discuss the relation between GC and the coupling strength S when there exists a synaptic connection between two neurons. Note that the STC $\epsilon_2^{\mathrm{A}}|_1(\tau)$ corresponds to the spike-induced change of ϵ_2^{A}. From the I&F system [e.g., See Eq. (23) in *Methods*], this change is asymptotically proportional to the coupling strength S when τ is small. Therefore, combined with Eqs. (13) and (14), we can make a connection that GC is quadratically related to the coupling strength as

$$F_{V_1\to V_2} \propto S^2. \tag{15}$$

Fig. 2M–O shows that, in three different dynamical regimes, there is an approximately quadratic relation between GC and the coupling strength, confirming the relationship in Eq. (15). Note that the two-neuron network we discussed above is for the unidirectional case. However, the above analytical derivations are still valid for the case of bidirectional connections.

It is worthwhile to emphasize that it is the δ-like noise structure of residuals, induced by the firing-reset dynamics, that links STC with the cross-correlation [Eq. (14)]. This is a crucial feature in the I&F dynamics that underlies why the GC connectivity can be captured by the STC on whitened signals. The approximate quadratic relationship between GC and S [Fig. 2M-O] ultimately underlies the coincidence between the causal and the structural connectivity for the I&F networks.

Further investigation of GC

As discussed above, by applying the GC analysis to voltage time series, we have obtained that the synaptic connectivity between neurons can be identified by the GC connectivity for the I&F networks. We now turn to the further investigation of the following issues: (i) whether the synaptic connectivity between a single neuron and a subnetwork or the connectivity between subnetworks can also be revealed by the GC connectivity; (ii) whether the GC connectivity constructed by merely using the spike train time series is also coincident with the synaptic connectivity; (iii) for more realistic neurons, e.g., the exponential I&F model, whether there is also a direct connection between synaptic connectivity and GC connectivity; (iv) for networks with both excitatory and inhibitory neurons, whether the network topology can also be successfully reconstructed by the GC analysis.

GC connectivity for subnetworks. In extracellular recording, the microelectrode is usually placed away from individual neurons, allowing the activity of a large number of neurons to contribute to the measured signal. We model the signal extracted from such extracellular microeletrodes, i.e., local field potential, by using the voltage averaged over population of neurons and we will term this as the voltage of subnetworks.

For a nine-neuron network [Figs. S1(A) and S2(A)], we can divide it into one subnetwork and one single neuron, where the single neuron corresponds to one neuron in the original network and the subnetwork corresponds to the remaining eight neurons. Through this division, we can construct an effective two-"neuron" that consists of the subnetwork as an effective neuron and the other neuron as another [Fig. S1(C) and S2(C)]. We compute the GC of this effective two-"neuron" network using the voltage of the subnetwork and the voltage of the single neuron [as displayed in Fig. S1(D) and S2(D)]. Our results show that the GC connectivity can successfully capture the structural connectivity between the subnetwork and the single neuron. This reconstruction holds for the case of a subnetwork presynaptic to a single neuron and vice versa (Figs. S1 and S2).

We further examine whether the synaptic connectivity between subnetworks can be revealed by the GC analysis. For a fifteen-neuron network [Fig. S3(A)], we divide this fifteen-neuron network into three subnetworks and construct an effective three-"neuron" network [Fig. S3(C)]. For this effective network consisting of three subnetworks, there are connections that are both "presynaptic" and "postsynaptic" between some subnetworks and there are also "presynaptic" connections only from one subnetwork to another subnetwork. Using voltage time series of these three subnetworks, we compute the GC connectivity [Fig. S3(D)]. Our results show that the GC connectivity is the same as the structural connectivity between subnetworks. From these results, we can conclude that the synaptic connectivity between subnetworks can also be correctly identified by the corresponding GC connectivity.

GC connectivity via spike trains. We have so far demonstrated that the GC analysis is effective to reconstruct anatomical connectivity within a network by using continuous-valued signals, e.g., voltage time series. Compared with voltage signals, the recent advent of multiple-electrode recording has made it comparatively easy to simultaneously record spiking activity (action potential) of multiple neurons [65–67]. The neuronal activity can often be described by a train of spike events [57,68,69],

$$S_i(t)=\sum_k \delta(t-T_{i,k}), \tag{16}$$

where $T_{i,k}$ is the kth spike of the ith neuron. The spike train can also be characterized as a binary vector with a component chosen as 1 if a spike has occurred in the sample interval, and chosen as 0 otherwise [70]. Such time series present theoretical challenges because most standard signal processing techniques are designed primarily for continuous-time processes instead of point processes [71].

There are some methods which have already been developed to identify causal relationships between spike trains of simultaneously recorded multiple neurons in experiment. For instance, under the assumption of stationarity, a nonparametric frequency domain approach was proposed to estimate GC directly from the Fourier transforms of spike train data [72–74]. Some other statistical methods based on information theory or likelihood function have also been put forth and applied to the analysis of sensory and motor data collected from experiments [75–78]. Here, we focus on the time domain GC analysis and study whether the anatomical connectivity of the I&F networks can also be directly mapped to the GC connectivity obtained by using spike train data. Note that, this GC analysis is different than using voltage time series. Unlike voltage data which are continuous-valued data, the spike train data are point-process data and it remains to be determined whether these data can be well described by the multivariate autoregressive models [78].

Following the algorithm of the GC analysis, we use spike train time series (binary vector as described above) to construct the causal connectivity network for the I&F neuronal systems and compare with their structural connectivity. For the two-neuron network as shown in Fig. 1A, we scan the parameters f and μ in Poisson input to cover different dynamical regimes and the range of firing rates of realistic neurons. Our results [Fig. S4(A)] show that the synaptic connectivity between two neurons can be well captured by the causal connectivity. For the hundred-neuron network as shown in Fig. 3A, we compute the causal adjacency matrix $\boldsymbol{G}$ and compare it with the synaptic adjacency matrix $\boldsymbol{A}$. Our results [Fig. S4(B)] again demonstrate that $\boldsymbol{A}$ can be successfully reconstructed by $\boldsymbol{G}$ with very high accuracy ($\geq 99.5\%$). Similarly, as for the case of GC from voltage time series, there is also a gap when we rank the GC by magnitude for all possible directed connections between neurons. Using a horizontal line [(blue online) in Fig. S4(C)] that divides the GC values into two groups, we can obtain $\boldsymbol{G}=\boldsymbol{A}$ with 100% accuracy by using this horizontal line as the GC threshold F_{T}.

To demonstrate that our previous analysis of the mechanism underlying the successful reconstruction by using voltage time series for the I&F networks can also be extended to that using spike train time series, we examine the relation between the regression coefficients $\hat{b}_k^{\mathrm{J}}$, $\hat{c}_k^{\mathrm{J}}$ and the residual cross-correlation r_k, r_{-k} as in Eqs. (12) for the two-neuron network in Fig. 1A. Our results [Fig. S5(A) – (C)] show that the relation [Eqs. (12)] between the regression coefficients and the residual cross-correlation holds very well when the GC connectivity is obtained by using spike train time series. Our results show that there is a vanishing coefficient $\hat{b}_k^{\mathrm{J}}$, i.e., no causal influence from neuron 2 to neuron 1, and a nonvanishing $\hat{c}_k^{\mathrm{J}}$, i.e., there is causal influence from neuron 1 to neuron 2. This is also consistent with the synaptic connectivity of the two-neuron network as shown in Fig. 1A. Similarly, due to the δ-like structure of residuals, we can also obtain that the GC constructed from spike train time series is quadratically related to the coupling strength [as verified in Fig. S5(D) – (F)].

GC for exponential integrate-and-fire neuronal networks. To present evidence that our results are not restricted to the standard I&F model [See Eq. (23) in *Methods*], which does not contain spike generation dynamics, we further carry out the GC analysis for the exponential integrate-and-fire (EI&F) neuronal model [See Eq. (24) in *Methods*]. The EI&F model captures the action potential of real neurons in a biophysically motivated way by fitting the spike-onset region to realistic neurons, such as the conductance-based Wang-Buzsaki model [79–81]. Compared with the standard I&F model which combines linear filtering of input currents with a strict voltage threshold, the EI&F model allows a replacement of the strict voltage threshold by a relatively realistic smooth spike initiation zone [82,83]. The model can quite faithfully reproduce response properties of the Hodgkin-Huxley type neurons under rapidly fluctuating inputs [84,85].

Using the voltage time series obtained by numerically evolving the system of EI&F neurons [See Eq. (24) in *Methods*], we construct regression models for these simulated data and compute causal connectivity of EI&F neuronal networks through the GC analysis. We perform the reconstruction [Fig. S6(A)] for the two-neuron network with the synaptic connectivity shown in Fig. 1A by scanning the parameters f and μ. Our results demonstrate that the reconstruction is successful for almost all choices of parameters over different dynamical regimes and with the range over the firing rate ($5\sim150$ Hz) of real neurons [35,57]. For the reconstruction of the hundred-neuron network with its synaptic connectivity shown in Fig. 3A, the difference between the synaptic adjacency matrix $\boldsymbol{A}$ and the constructed causal adjacency matrix **G** is small [Fig. S6(B)]. We can still obtain a very high accurate reconstruction ($\geq 99\%$). Interestingly, if we rank all GC values in order of magnitude for this hundred-neuron network, as for the case of I&F models, there is also a gap [Fig. S6(C)]. Any horizontal line in the gap [e.g., the blue line in Fig. S6(C)] can be naturally used as a GC threshold F_{T} to divide the GC values into two groups, yielding the result $\boldsymbol{G}=\boldsymbol{A}$ with 100% accuracy.

In comparison with the I&F model, the EI&F neuronal model contains an extra spike-generating current term $\psi_i(V)$ which takes the form of an exponential function. Note that $\psi_i(V)$ is almost negligible when the voltage of the neuron is below the spike-initiation threshold V_T. If the neuron fires, $\psi_i(V)$ will be dominant and the membrane potential will grow exponentially fast to infinity. After that, the voltage of the neuron will be reset to the reset value. Therefore, the EI&F neuron also possesses the same firing-reset dynamics as the I&F neuron and our previous analysis, e.g., Eqs. (12) and (15), should also be valid for this more realistic neuronal model. To confirm this, we have verified the relation [Eqs. (12)] between regression coefficients and residual cross-correlations for the two-neuron network in Fig. 1A [as shown in Fig. S7(A) – (C)], and Eqs. (12) is indeed valid for the EI&F model. Similarly, as for the case of I&F model, we have a vanishing coefficient $\hat{b}_k^{\mathrm{J}}$, i.e., there is no causal influence from neuron 2 to neuron 1, and a nonvanishing $\hat{c}_k^{\mathrm{J}}$, i.e., there is a causal influence from neuron 1 to neuron 2. This is again consistent with the underlying synaptic connectivity between the two neurons as shown in Fig. 1A. By using the δ-like structure of residuals for the EI&F networks, we can also obtain that GC is quadratically related to the coupling strength as in Eq. (15). This result has also been numerically verified [Fig. S7(D) – (F)].

GC for excitatory and inhibitory neuronal networks. Finally, we address the issue of whether the above reconstruction can be extended to networks with both excitatory and inhibitory neurons (See Eq. (25) in *Methods*). For a two-neuron network with one excitatory and one inhibitory neurons as shown in Fig. 5A, there is only a unidirectional inhibitory synaptic connection from the inhibitory neuron 1 to the excitatory neuron 2. We scan the parameters of Poisson input and compare the synaptic adjacency matrix $\boldsymbol{A}$ and the constructed causal adjacency matrix $\boldsymbol{G}$. As shown in Fig. 5C, $\boldsymbol{G}$ is also highly coincident with $\boldsymbol{A}$ over a wide range of dynamical regimes. For a three-neuron network with two excitatory neurons and one inhibitory neuron as shown in Fig. 5B, there are both excitatory and inhibitory synaptic connections within this small network. By scanning the parameters of Poisson input as shown in Fig. 5D, we also obtain successful reconstruction of the synaptic connectivity $\boldsymbol{A}$ from the causal connectivity $\boldsymbol{G}$ over a wide range of dynamical regimes.

In addition, we have also considered a hundred-neuron network with 80 excitatory and 20 inhibitory neurons. The synaptic connectivity for this hundred-neuron network is chosen to be the same as that in Fig. 3A. The difference between the synaptic adjacency matrix $\boldsymbol{A}$ and the constructed causal adjacency matrix $\boldsymbol{G}$ is displayed in Fig. 5E. It can be seen that the accuracy of reconstruction is still very high ($\geq 95\%$). Similarly, we also rank the GC values in order of magnitude and find that, unlike the network with only excitation, there is no clear gap which can naturally divide the GC values into two groups (Fig. 5F). For the GC reconstruction of the network with both excitatory and inhibitory neurons, it is also important to infer the connection type, i.e., excitatory or inhibitory, in addition to the inference of the presence of the connection, and this issue warrants further investigations in the future.

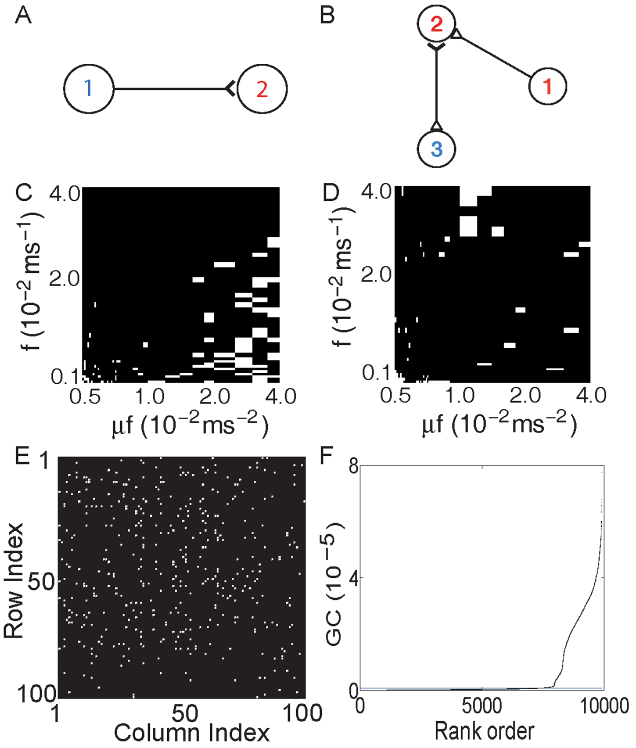

Figure 5. GC connectivity for networks with both excitation and inhibition. Illustrated here are results related to two-neuron and three-neuron I&F networks with both excitation and inhibition in (A) – (D), and a large network in (E) and (F). The edge with "◁" or "<" at the end signifies the directed excitatory or inhibitory connections, respectively. The input parameters are chosen as $\mu=0.24\ \mathrm{ms}^{-1}$ (Poisson input rate) and $f=0.02\ \mathrm{ms}^{-1}$ (Poisson input strength). (A) a two-neuron network with one inhibitory neuron (labeled by neuron 1) and one excitatory neuron (labeled by neuron 2). There is only a unidirectional inhibitory synaptic connection from neuron 1 to neuron 2. (B) a three-neuron network with two excitatory neurons (labeled by neuron 1 and 2) and one inhibitory neuron (labeled by neuron 3). There are two excitatory synaptic connections as from neuron 1 to neuron 2 and from neuron 2 to neuron 3. There is also one inhibitory synaptic connection from neuron 3 to neuron 2. (C) The coincidence between $\boldsymbol{A}$ and $\boldsymbol{G}$ for the two-neuron network in (A). (D) The coincidence between $\boldsymbol{A}$ and $\boldsymbol{G}$ for the three-neuron network in (B). The white color indicates that $\boldsymbol{A}\neq\boldsymbol{G}$, whereas the black color for $\boldsymbol{A}=\boldsymbol{G}$. (E) The absolute difference between $\boldsymbol{A}$ and $\boldsymbol{G}$, i.e., $|A_{ij}-G_{ij}|$ for the large network with 80 excitatory and 20 inhibitory neurons with adjacency matrix shown in Fig. 3A. The white color indicates that $|A_{ij}-G_{ij}|=1$, namely, $A_{ij}\neq G_{ij}$ and the black color for $A_{ij}=G_{ij}$. The percentage of total connections (number of nonzero A_{ij}) is $\sim 20\%$ and the average neuronal firing rate is ~ 10 Hz. By significance test ($p=0.001$, See Text S1 for more details), the total number of $A_{ij}\neq G_{ij}$ is 412 out of $\sim 10{,}000$ possible pairs of connections. (F) Ranked GC in order of magnitude with the line (blue online) indicating a threshold obtained from the above significance test. Here, the coupling strength from excitatory to excitatory neuron S_{EE} and from excitatory to inhibitory neuron S_{IE} are $S_{EE}=S_{IE}=0.006\ \mathrm{ms}^{-1}$ (corresponding EPSP is 0.6 mV), whereas the coupling strength from inhibitory to excitatory neuron S_{EI} and from inhibitory to inhibitory neuron S_{II} are $S_{EI}=S_{II}=0.01\ \mathrm{ms}^{-1}$ (the corresponding IPSP is ~ 0.3 mV).

doi:10.1371/journal.pone.0087636.g005

Discussion

We have shown that the linear GC framework with either continuous voltage or discrete spike train time series, can be successfully applied to the reconstruction of I&F-type neuronal networks. For such nonlinear networks, the causal connectivity obtained by the GC algorithm with sufficiently long time series corresponds well to their synaptic connectivity. In our simulations, we choose the data length of recording activity to be $\sim 20\,\mathrm{mins}$ [86–88] to ascertain that the statistical error is sufficiently small over a wide range of dynamical regimes. However, in real experiments, there may be many complications to maintain the stationarity of neuronal activity with such a long duration of recording [9]. Therefore, we investigate whether the GC reconstruction can be achieved, with high accuracy, within a realistic range of recording length in experiment. For the two-neuron network as shown in Fig. 1, we have investigated how the minimal data length required for GC reconstruction (See Text S1 for more details) using either voltage or spike train time series depends on neuronal firing rate. As shown in Fig. S8(A) and (C), the minimal data length for a successful GC reconstruction by using voltage time series can be as short as ~ 1 min for both spontaneous firing rate (less than 1 Hz) and the high firing rate range (above 20 Hz). In contrast, the minimal data length for GC reconstruction by using spike train time series appears to be monotonically dependent on the neuronal firing rate as shown in Fig. S8(B) and (D). When the firing rate is sufficiently high, e.g., above 20 Hz, the required minimal length can be as short as a few seconds. However, if a spontaneous firing rate is sufficiently low, e.g., less than 1 Hz, the minimal data length required for the GC reconstruction can be as long as 20 mins. This is somewhat expected because for the GC reconstruction using spike train time series (digital signals), the correlation structure between neurons, as captured by GC influence, can only be reflected by their spikes. If the neuronal firing rate is low, it takes a long time to accumulate a sufficient number of spikes to obtain statistical information of the correlation structure between neurons. However, for the GC reconstruction using voltage time series, the causal influence can be reflected by both subthreshold and suprathreshold (spike) dynamics. Therefore, it may not need that long time to obtain statistical correlation information even if the firing rate is low. Another phenomenon is that the required data length will be shorter if the Poisson input strength becomes smaller. This phenomenon can be clearly seen in Fig. S8 as indicated by the red curve (lower f), in general, being lower than the blue curve (higher f). This is also intuitively reasonable since the statistical fluctuations may also decrease when the background input becomes weaker while the coupling strength between neurons is fixed.

The computational cost of GC algorithm can be estimated to be $O(mLN^2)+O(m^3N^4)$, where L is the data length, N is the total neuron number and m is the regression order in the regression models (See *Methods* for more details). The first term describes the computational cost of covariance matrices and the second term corresponds to the computational cost arising from solving Yule-Walker equations (There are some more efficient algorithms, such as Levinson, Euclidean and Berlekamp-Massey algorithms, which can solve the Yule-Walker equations with $O(N^2)$ arithmetic operations). Furthermore, we have established a quantitative relationship among the GC, the STC and the coupling strength. Our theoretical analysis based on voltage time series can be naturally extended to the case of spike trains time series and our results show that the GC tool can be directly applied to point-process data [74,78]. Therefore, the linear GC technique can be potentially used to detect the underlying synaptic connections within a neuronal network by measuring either the voltage trajectories or the spike trains of neurons. We note in passing that the GC reconstruction does not perform well in some cases as shown by the white color region in Fig. 1E–F and Fig. 5C–D. It appears that the statistical error is still not sufficiently small in these cases. We have also examined the dependence of performance of GC reconstruction on the density of the connection matrix. For the case of low density connections (less than 20%) as shown in Figs. 3,5, and 6, the GC reconstruction has a very high accuracy. This indicates the GC reconstruction could potentially be applied to the cortical network reconstruction since many studies have indicated that the structural brain connectivity forms a sparse graph [22,89]. It appears that for a network of high density connections, e.g., greater than 50%, the GC reconstruction does not perform as well, e.g., with approximately 70% accuracy of reconstruction. We suspect that this could be related to the fact that the signal-to-noise ratio for each pair of coupling to be out of the dense coupling pool is much lower for a network with dense connections than that with sparse connections. A further systematic investigation is warranted to achieve a full understanding of this issue in the future.

In addition, we have shown that the synaptic connection in some coarse-grained sense, e.g., the connection between an individual neuron and a subnetwork, or the connection between subnetworks, can also be recovered through GC analysis. In our work, the recorded time series of a subnetwork is the voltage response averaged over neurons within the subnetwork, which can be viewed as a model for the local field potential (LFP). Note that the LFP in our case includes both the subthreshold dynamics and the spike-reset dynamics, and it may be different from the LFP normally measured in experiment, which contains only a low-pass filtered component of population voltages [90]. As for the

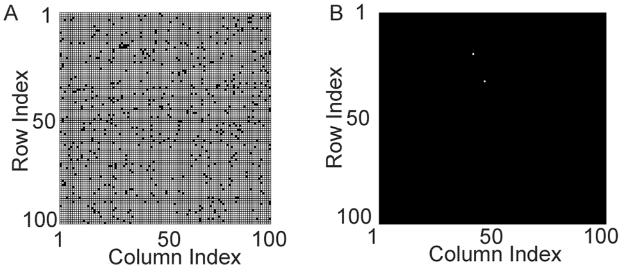

Figure 6. GC reconstruction for a large network with low density connections. Illustrated here are results for a large I&F network (80 excitatory and 20 inhibitory neurons) with random connectivity. The indices from 1 to 80 are for excitatory neurons and the indices from 81 to 100 are for inhibitory neurons. The total number of nonzero A_{ij} is 531 (the percentage of connections is $\sim 5\%$) and the average neuronal firing rate is ~ 50 Hz. (A) The synaptic adjacency matrix $A=(A_{ij})$ with the white color indicating that $A_{ij}=0$ and the black color for $A_{ij}=1$. (B) The absolute difference between A and the causal adjacency matrix G, i.e., $|A_{ij}-G_{ij}|$. The white color indicates that $|A_{ij}-G_{ij}|=1$, namely, $A_{ij}\neq G_{ij}$ and the black color for $A_{ij}=G_{ij}$. By significance test ($p=0.0002$, See Text S1 for more details), the total number of $A_{ij}\neq G_{ij}$ is 2 out of $\sim 10{,}000$ possible pairs of connections. Parameters are chosen as $\mu=1.0\,\mathrm{ms}^{-1}$ (Poisson input rate), $f=0.012\,\mathrm{ms}^{-1}$ (Poisson input strength), the coupling strength from excitatory to excitatory neuron S_{EE} and from excitatory to inhibitory neuron S_{IE} are $S_{EE}=S_{IE}=0.005\,\mathrm{ms}^{-1}$ (the corresponding EPSP is ~ 0.5 mV), whereas the coupling strength from inhibitory to excitatory neuron S_{EI} and from inhibitory to inhibitory neuron S_{II} are $S_{EI}=S_{II}=0.007\,\mathrm{ms}^{-1}$ (corresponding to IPSP ~ 0.2 mV).
doi:10.1371/journal.pone.0087636.g006

averaged voltage response processed by a low-pass filter, our conclusions can still be valid as long as the low-pass filter is chosen to be a causal filter, namely, the filter output depends only on past and present inputs. The reason can be explained as follows: if the averaged voltage response (AVR) is processed by a causal low-pass filter, then the transformation between the filtered AVR and the original AVR is linear and invertible. The GC is invariant under such filtering because of the invariance of GC under invertible linear transformation [44,45]. In fact, the filtered AVR is different from the original AVR. However, the residual of auto regression for the filtered AVR is only different from that for the original AVR by a factor if the filter is chosen to be a causal filter. Therefore, the corresponding structure of both the residual cross-correlation and the STC on residuals are the same as those of the original AVR (although the amplitude may be different by a factor). As a result, our conclusions about network reconstruction and our theoretical analysis remain valid.

There are other important issues that remain to be fully elucidated in the future. One of them is whether an accurate reconstruction can still be obtained when the inputs to neurons are correlated. For instance, it is quite common that a pair of neurons may receive a common synaptic input from another neuron [91–93]. Our study shows that an approximate reconstruction can be achieved (with an accuracy greater than 70%) if the correlation coefficient for two input spike trains is less than 10% [94]. As an illustration of how the success of GC reconstruction depends on the input correlation, we have studied the effects of input correlation on the GC reconstruction by using either voltage or spike train time series for the two-neuron network as shown in Fig. 1A. In addition to its own Poisson input (independent of each other) with the same rate μ and the same strength f, each neuron in the network receives a common Poisson input with rate μ_0 and strength f. The percentage of common Poisson input P_{common} is defined by $\mu_0/(\mu+\mu_0)$. As discussed previously, a successful GC reconstruction for the synaptic connectivity of this network indicates that the GC from neuron 1 to neuron 2 ($F_{V_1\to V_2}$ or $F_{S_1\to S_2}$) is significantly nonzero, whereas the GC from neuron 2 to neuron 1 ($F_{V_2\to V_1}$ or $F_{S_2\to S_1}$) nearly vanishes. Therefore, the GC ratios $F_{V_1\to V_2}/F_{V_2\to V_1}$ and $F_{S_1\to S_2}/F_{S_2\to S_1}$ can be used as a measure of quantifying how successful GC reconstructions are. As shown in Fig. S9, we plot such GC ratios as a function of P_{common}. It can be seen from Fig. S9 that the magnitude of both GC ratios drops rapidly as P_{common} increases, thus indicating that the GC reconstruction eventually fails when P_{common} is large. However, as shown in Fig. S9, the GC reconstruction can still be trusted if the percentage of common Poisson input is less than 10% because there is about one order of magnitude difference between $F_{V_1\to V_2}$ ($F_{S_1\to S_2}$) and $F_{V_2\to V_1}$ ($F_{S_2\to S_1}$).

Another issue is related to the synchronization among neurons [95]. We have found that, for a nearly (not fully spike-to-spike) synchronized regime, the reconstruction can be achieved by refining sampling. It is obvious that the drive-response scenario, which the GC theory addresses, would be difficult to disentangle when the neuronal network falls into the spike-to-spike synchronized dynamical regime [95–98]. In such cases, the causal influences between neurons would decrease, whereas the instantaneous causality would increase [14]. As for the sampling rate used in our simulations, we choose $\sim 2\,\text{kHz}$ for our sampling rate (the time scale of refractory period in our neuronal models is $\sim 2\,\text{ms}$, therefore, the sampling rate should be chosen larger than $500\,\text{Hz}$ to capture this time scale). In addition, we have also examined different sampling rates between $1\,\text{kHz}$ and $2\,\text{kHz}$ and found that the structural connectivity can always be revealed by GC connectivity with similar high accuracy.

Finally, we point out that there are some other methods that have been developed to reconstruct the network topology, e.g., phase resetting or chaotic synchronization [99–107]. These techniques were applied to either coupled oscillators or current-based networks [108], which can be regarded as the reduced form of the general conductance-based I&F networks. For instance, in the limit $\sigma\to 0$, $\mu\to\infty$ and $\mu f=\text{const}$, the conductance-based I&F network reduces to Mirollo-Strogatz oscillators which are widely used in the study of synchronization phenomena [109]. Therefore, our work provides a general methodology to reconstruct the network topology for conductance-based I&F networks. In terms of the GC theory, there are also some extensions to investigate causal relationship for nonlinear and non-Gaussian time series, e.g., the kernel-Granger causality method [110,111]. The concept of such nonlinear GC is formulated by using the theory of reproducing kernel Hilbert spaces that are spanned by choosing proper kernel functions. The form of kernel functions relies on the nonlinearity of the original dynamical systems, which is usually unknown. In our work, if we choose the kernel function for I&F networks to be a bilinear function, then the nonlinear GC framework reduces to the linear GC framework. Our results have shown that such reduced nonlinear GC analysis is able to capture well the underlying topology of I&F networks.

Methods

Granger Causality (GC) Analysis

We first recall theoretical definitions of GC for time series in the bivariate case and the conditional GC for time series in the multivariate case (In the discussion of GC, we will always assume that the mean of time series has been subtracted and the expectations of time series for both bivariate and multivariate cases are zero). The idea of GC was formalized in the context of linear regression models [43,112]. Specifically, if the variance of the prediction error of the first time series in the auto regressive model is reduced by incorporating the knowledge of the second one, then the second time series is said to have a causal influence on the first one [44,45]. The roles of the two time series can be reversed to address the question of causal influence in the opposite direction. The GC theory has been widely applied to many research fields as mentioned in *Introduction* [14,46].

Bivariate case. For two time series $x_1(t)$ and $x_2(t)$, their auto regression (AR) models can be represented by

$$\begin{aligned} x_1(t) &= \sum_{k>0} a_k^{\text{A}} x_1(t-k)+\epsilon_1^{\text{A}}(t), \\ x_2(t) &= \sum_{k>0} d_k^{\text{A}} x_2(t-k)+\epsilon_2^{\text{A}}(t), \end{aligned} \tag{17}$$

where ϵ_1^{A} and ϵ_2^{A} are residuals (prediction errors) of AR processes for x_1 and x_2, respectively. To illustrate GC relations between $\{x_1(t)\}$ and $\{x_2(t)\}$, we further consider their joint regression (JR) models as

$$\begin{aligned} x_1(t) &= \sum_{k>0} a_k^{\text{J}} x_1(t-k)+\sum_{k>0} b_k^{\text{J}} x_2(t-k)+\epsilon_{1,2}^{\text{J}}(t), \\ x_2(t) &= \sum_{k>0} c_k^{\text{J}} x_1(t-k)+\sum_{k>0} d_k^{\text{J}} x_2(t-k)+\epsilon_{2,1}^{\text{J}}(t), \end{aligned} \tag{18}$$

where $\epsilon_{1,2}^{\text{J}}$ is the residual of JR process for x_1 by further incorporating the history of x_2, and $\epsilon_{2,1}^{\text{J}}$ is the residual of JR process for x_2 by further incorporating the history of x_1 [14,113]. By assuming that x_1 and x_2 are wide-sense stationary, i.e., their means and variances are constants, the GC from x_2 to x_1, denoted by $F_{x_2 \to x_1}$, and that from x_1 to x_2, denoted by $F_{x_1 \to x_2}$ are defined as

$$F_{x_2 \to x_1} = \ln \frac{\mathrm{Var}(\epsilon_1^{\mathrm{A}})}{\mathrm{Var}(\epsilon_{1,2}^{\mathrm{J}})} \quad \text{and} \quad F_{x_1 \to x_2} = \ln \frac{\mathrm{Var}(\epsilon_2^{\mathrm{A}})}{\mathrm{Var}(\epsilon_{2,1}^{\mathrm{J}})}, \tag{19}$$

where $\mathrm{Var}(\epsilon_1^{\mathrm{A}})$ and $\mathrm{Var}(\epsilon_2^{\mathrm{A}})$ are the variances of the residuals ϵ_1^{A} and ϵ_2^{A} in AR models, respectively. These variances quantify the accuracy of the autoregressive prediction of x_1 and x_2 at the present moment based on their own past. The quantities $\mathrm{Var}(\epsilon_{1,2}^{\mathrm{J}})$ and $\mathrm{Var}(\epsilon_{2,1}^{\mathrm{J}})$ are the variances of the residuals $\epsilon_{1,2}^{\mathrm{J}}$ and $\epsilon_{2,1}^{\mathrm{J}}$ in JR models, respectively. They represent the accuracy of predicting the present value of x_1 or x_2 based on the previous values of both x_1 and x_2 [44,45]. For instance, if $\mathrm{Var}(\epsilon_{1,2}^{\mathrm{J}})$ is less than $\mathrm{Var}(\epsilon_1^{\mathrm{A}})$, then there is an improvement in the prediction of x_1 by incorporating the history of x_2, thus x_2 is said to have a causal influence on x_1. Note that, both $F_{x_2 \to x_1}$ and $F_{x_1 \to x_2}$ cannot be negative by definition. In particular, $F_{x_2 \to x_1} = 0$ $[F_{x_1 \to x_2} = 0]$ corresponds to the situation where there is no causal influence from x_2 $[x_1]$ to x_1 $[x_2]$ [14,44].

Multivariate case. In the case of multivariate time series $\{x_i(t)\}_{i=1}^N$ $(N > 2)$, the causal relation between two time series, say, $x_1(t)$ and $x_2(t)$, can be directly mediated or it can be indirectly mediated by a third one, say $x_3(t)$. However, the above pairwise analysis for the bivariate case cannot distinguish whether the causal influence between x_1 and x_2 is direct or indirect [14]. The framework of conditional Granger causality was developed to address such situations [45]. The procedure can be carried out as follows: for any two time series $x_i(t)$ and $x_j(t)$ among the set $\{x_i(t)\}_{i=1}^N$, the conditional AR processes are represented by

$$\begin{aligned} x_i(t) &= \sum_{l>0} a_{i,l}^{\mathrm{A}} x_i(t-l) + \sum_{k \neq i,j}^{N} \sum_{l>0} a_{k,l}^{\mathrm{A}} x_k(t-l) + \epsilon_i^{\mathrm{A}}(t), \\ x_j(t) &= \sum_{l>0} d_{j,l}^{\mathrm{A}} x_j(t-l) + \sum_{k \neq i,j}^{N} \sum_{l>0} d_{k,l}^{\mathrm{A}} x_k(t-l) + \epsilon_j^{\mathrm{A}}(t), \end{aligned} \tag{20}$$

where "conditional" means the auto regressions of $x_i(t)$ and $x_j(t)$ are performed when the history of all other time series $\{x_k(t)\}$ $(k \neq i,j)$ is given. Furthermore, we consider the conditional JR processes for $x_i(t)$ and $x_j(t)$ as

$$\begin{aligned} x_i(t) &= \sum_{l>0} a_{i,l}^{\mathrm{J}} x_i(t-l) + \sum_{l>0} b_{j,l}^{\mathrm{J}} x_j(t-l) + \sum_{k \neq i,j}^{N} \sum_{l>0} a_{k,l}^{\mathrm{J}} x_k(t-l) + \epsilon_{i,j}^{\mathrm{J}}(t), \\ x_j(t) &= \sum_{l>0} c_{i,l}^{\mathrm{J}} x_i(t-l) + \sum_{l>0} d_{j,l}^{\mathrm{J}} x_j(t-l) + \sum_{k \neq i,j}^{N} \sum_{l>0} d_{k,l}^{\mathrm{J}} x_k(t-l) + \epsilon_{j,i}^{\mathrm{J}}(t). \end{aligned} \tag{21}$$

From Eqs. (20) and (21), the conditional GC from x_j to x_i, denoted by $F_{x_j \to x_i | \{x_k\}_{k \neq i,j}}$, and that from x_i to x_j, denoted by $F_{x_i \to x_j | \{x_k\}_{k \neq i,j}}$, are defined as

$$\begin{aligned} F_{x_j \to x_i | \{x_k\}_{k \neq i,j}} &= \ln \frac{\mathrm{Var}(\epsilon_i^{\mathrm{A}})}{\mathrm{Var}(\epsilon_{i,j}^{\mathrm{J}})} \quad \text{and} \\ F_{x_i \to x_j | \{x_k\}_{k \neq i,j}} &= \ln \frac{\mathrm{Var}(\epsilon_j^{\mathrm{A}})}{\mathrm{Var}(\epsilon_{j,i}^{\mathrm{J}})}. \end{aligned} \tag{22}$$

Note that, in Eqs. (20) and (21), both the auto and joint regressions of $x_i(t)$ and $x_j(t)$ are performed by including the history of other time series $x_k(t)$ $(k \neq i,j)$. Therefore, if the causal influence between x_i and x_j is entirely mediated by some other time series in the set $\{x_k(t)\}_{k \neq i,j}^N$, the variance of residuals in conditional AR models will be equal to the variance of residuals in conditional JR models, i.e., $\mathrm{Var}(\epsilon_i^{\mathrm{A}}) = \mathrm{Var}(\epsilon_{i,j}^{\mathrm{J}})$ and $\mathrm{Var}(\epsilon_j^{\mathrm{A}}) = \mathrm{Var}(\epsilon_{j,i}^{\mathrm{J}})$. Therefore, we have $F_{x_j \to x_i | \{x_k\}_{k \neq i,j}} = 0$ and $F_{x_i \to x_j | \{x_k\}_{k \neq i,j}} = 0$, that is, no further improvement in the prediction of $x_i(t)$ $[x_j(t)]$ in JR models can be expected by including past measurements of $x_j(t)$ $[x_i(t)]$. On the other hand, if the causal relation between $x_i(t)$ and $x_j(t)$, say from x_j to x_i, is direct, the inclusion of past measurements of $x_j(t)$ in addition to that of $x_i(t)$ and $\{x_k(t)\}_{k \neq i,j}^N$ will result in a better prediction of $x_i(t)$, thus leading to $\mathrm{Var}(\epsilon_{i,j}^{\mathrm{J}}) < \mathrm{Var}(\epsilon_i^{\mathrm{A}})$ and $F_{x_j \to x_i | \{x_k\}_{k \neq i,j}} > 0$.

GC algorithm for I&F networks

Here, for an I&F network with N neurons, we propose the following numerical algorithm of computing GC through the voltage time series of neurons (similarly for the case of using spike train time series). We denote the voltage trajectory of the ith neuron by $V_i(t)$, and the GC from the jth neuron to the ith neuron, obtained from these voltage time series, by $F_{V_j \to V_i}$. According to the above definition of GC, we compute both regression residuals ϵ_i^{A} and $\epsilon_{i,j}^{\mathrm{J}}$ as in Eqs. (20) and (21) to obtain $F_{V_j \to V_i}$ in Eq. (22). Note that the GC from the jth neuron to itself is always zero by definition (For neuronal systems discussed in our work, we do not consider autapses in the network). The flow of the algorithm to compute each $F_{V_j \to V_i}$ for every pair of neurons, where $i,j = 1,2,\cdots,N$ and $i \neq j$, can be described as follows (See Text S1 for more details):

Step 1: Evolve the I&F network dynamics [e.g., Eq. (23) in *Methods*] numerically and record the voltage signal averaged over each small time window ($\sim$0.5ms, i.e., sampling rate is 2 kHz) to form voltage time series of N neurons as $\{V_i(t)\}_{i=1}^N$, $t = 1,2,\cdots,L$. In most of our simulations, L is chosen to be 2.0×10^6, which corresponds to the length of time series $\sim$20 mins. Then, construct an N dimensional vector $\boldsymbol{X}_t = [\hat{V}_1(t), \hat{V}_2(t), \cdots, \hat{V}_N(t)]^T$ and $N-1$ dimensional vectors $\boldsymbol{X}_t^{(j)} = [\hat{V}_1(t), \hat{V}_2(t), \cdots, \hat{V}_{j-1}(t), \hat{V}_{j+1}(t), \cdots, \hat{V}_N(t)]^T$ for $j = 1,2,\cdots,N$, where $\hat{V}_i(t) = V_i(t) - \mathbb{E}[V_i(t)]$ has zero mean and the superscript (j) in $\boldsymbol{X}_t^{(j)}$ denotes the fact that the jth component $\hat{V}_j(t)$ in $\boldsymbol{X}_t$ is removed.

Step 2: For any given regression order $\hat{m} \geq 1$, compute the covariance matrix functions $\mathrm{C}_k = \langle \mathrm{X}_t \mathrm{X}_{t+k}^T \rangle_t = \frac{1}{L-\hat{m}} \sum_{t=1}^{L-\hat{m}} \boldsymbol{X}_t \boldsymbol{X}_{t+k}^T$ for $k = 0,1, \cdots, \hat{m}-1$ to construct the Yule-Walker equations. We denote the coefficient matrix and the right hand side of the Yule-Walker equations by $\boldsymbol{\Omega}_{\hat{m} \times \hat{m}}$ and $\boldsymbol{B}_{\hat{m}}$, respectively [Eqs. (4) – (7) in Text S1]. Solve the Yule-Walker equations to obtain the regression coefficients, which are denoted by $\Lambda_{\hat{m}}$ [Eq. (6) in Text S1]. Then, substitute $\Lambda_{\hat{m}}$ into the regressive equations [Eq. (1) in Text S1] to obtain the residual vector $\boldsymbol{E}_{(\hat{m})}(t) = [\epsilon_1^{(\hat{m})}(t), \epsilon_2^{(\hat{m})}(t), \cdots, \epsilon_N^{(\hat{m})}(t)]^T$ and calculate its covariance matrix, which is denoted by $\Sigma_{\hat{m}}$ [Eq. (2) in Text S1].

Step 3: Now, for each $\hat{m} \geq 1$, we have $\Sigma_{\hat{m}}$, therefore, we can obtain the BIC function [Eq. (10) in Text S1] as a function of $\hat{m}$. Use the BIC criterion to find the correct regression order $m \in \{\hat{m}\}$ which corresponds to the situation where the BIC function reaches its minimum.

Step 4: Then, choose $\hat{m}=m$ and return to Step 2 to obtain the residual vector $\boldsymbol{E}_{(m)}(t)$ and also the covariance matrix Σ_m. The ith diagonal element of Σ_m, denoted by $\Sigma_m(i,i)$, corresponds to $\mathrm{Var}(\epsilon_{i,j}^{\mathrm{J}})$, which is the variance of the residual $\epsilon_{i,j}^{\mathrm{J}}$ in the joint regression model of the ith neuron by incorporating the information of the jth neuron ($j=1,2,\cdots,N$) in addition to all other kth neurons ($k=1,2,\cdots,N$ and $k\neq i,j$). Set $\mathrm{Var}(\epsilon_{i,j}^{\mathrm{J}})=\Sigma_m(i,i)$, for different $i,j=1,2,\cdots,N$.

Step 5: Let $\hat{m}=m$ and use $\boldsymbol{X}_t^{(j)}$ for each j ($j=1,2,\cdots,N$) to follow the procedure of Step 2 to obtain the residual vector $\boldsymbol{E}_{(m)}^{(j)}(t)$ and the covariance matrix $\Sigma_m^{(j)}$. If the neuron index $i\leq j$, the ith diagonal element $\Sigma_m^{(j)}(i,i)$ corresponds to $\mathrm{Var}(\epsilon_i^{\mathrm{A}})$, which is the variance of the residual ϵ_i^{A} in the AR model of the ith neuron by incorporating the information of all other neurons except the jth neuron, set $\mathrm{Var}(\epsilon_i^{\mathrm{A}})= \Sigma_m^{(j)}(i,i)$. Otherwise, for $i>j$, the $(i-1)$th diagonal element $\Sigma_m^{(j)}(i-1,i-1)$ corresponds to $\mathrm{Var}(\epsilon_i^{\mathrm{A}})$ and set $\mathrm{Var}(\epsilon_i^{\mathrm{A}})= \Sigma_m^{(j)}(i-1,i-1)$.

Step 6: Compute all the GC values $F_{V_j\rightarrow V_i}=\frac{\mathrm{Var}(\epsilon_i^{\mathrm{A}})}{\mathrm{Var}(\epsilon_{i,j}^{\mathrm{J}})}$ for all pairs of neurons, i.e., $i,j=1,2,\cdots,N$.

Integrate-and-fire (I&F) neuronal network

We consider an I&F network with N conductance-based, pulse-coupled, excitatory point neurons. Under a Poisson drive, its dynamics is governed by

$$\begin{aligned}\frac{dV_i}{dt} &= -G^L(V_i-\epsilon^L)-G_i(V_i-\epsilon^E),\\ \frac{dG_i}{dt} &= -\frac{G_i}{\sigma}+S\sum_{j\neq i}^{N}\sum_k A_{ij}\delta(t-T_{j,k})+I_{i,\mathrm{ext}},\end{aligned} \tag{23}$$

where the index i labels the ith neuron in the network. V_i is the membrane potential and G_i is the excitatory synaptic conductance. ϵ^E is the excitatory reversal potential. G^L and ϵ^L are the leaky conductance and the leaky reversal potential, respectively. The excitatory synaptic dynamics are described by G_i, which rises instantaneously upon receiving a spike and has a decay time scale σ. The voltage of the jth neuron V_j evolves continuously according to Eq. (23) until it reaches the firing threshold V_{th}, at which point the jth neuron is referred to as producing an action potential or emitting a spike (the time of the kth spike is recorded as $T_{j,k}$). Then, this spike triggers postsynaptic events in all the neurons that the jth neuron is presynaptically connected to and changes their conductances with the coupling strength S [the corresponding physiological excitatory postsynaptic potential (EPSP) is $\sim(100\times S\,\mathrm{ms})\mathrm{mV}$]. Here, the synaptic connectivity of the network is characterized by an adjacency matrix $A=(A_{ij})$, where $A_{ij}=1$ ($A_{ij}=0$) means the presynaptic jth neuron is connected (unconnected) to the postsynaptic ith neuron. Meanwhile, V_j after the jth neuron's spike is reset to the reset voltage V_{R} and is held at V_{R} for an absolute refractory period of τ_{ref} ms. Each neuron (say, the ith neuron) in the system is also driven by a stochastic feedforward input $I_{i,\mathrm{ext}}=f\sum_l\delta(t-T_{i,l}^F)$, a spike train sampled from a Poisson process with rate μ. We denote $T_{i,l}^F$ as the lth spike from the feedforward input to the ith neuron and the delta function associated with this spike instantaneously increases the ith neuron's conductance by magnitude f.

In comparison with the classical Hodgkin-Huxley (HH) neuronal model with detailed ionic currents to resolve the stereotypical spike dynamics [114], the model (23), as a reduced neuronal model, is much more efficient in terms of computation while capturing sufficiently rich network dynamics of HH models [58,59,96,115,116]. Therefore, it has been widely used in large-scale simulations to address information processing issues arising from neuronal systems [36–42]. In the reduced-dimensional units, in which only time retains dimensional, with units of conductance being $[\mathrm{ms}^{-1}]$, the parameters in the model (23) are chosen as [117]: $G^L=0.05\ \mathrm{ms}^{-1}$, $\epsilon^L=0$, $\epsilon^E=14/3$, $V_{\mathrm{th}}=1$, $V_R=0$, $\sigma=2$ ms, $\tau_{\mathrm{ref}}=2$ ms, which correspond to typical physiological values: $G^L=50\times10^{-6}\Omega^{-1}\mathrm{cm}^{-2}$, $\epsilon^L=-70$ mV, $\epsilon^E=0$ mV, $V_{\mathrm{th}}=-55$ mV.

Exponential integrate-and-fire (EI&F) neuronal network

The dynamics of an excitatory EI&F neuronal network with N neurons is governed by

$$\begin{aligned}\frac{dV_i}{dt} &= -G^L(V_i-\epsilon^L)-G_i(V_i-\epsilon^E)+\psi_i(V),\\ \frac{dG_i}{dt} &= -\frac{G_i}{\sigma}+S\sum_{j\neq i}^{N}\sum_k A_{ij}\delta(t-T_{j,k})+I_{i,\mathrm{ext}},\end{aligned} \tag{24}$$

where the function $\psi_i(V)=G^L\Delta_T\exp\left(\frac{V_i-V_T}{\Delta_T}\right)$ characterizes the spike-generating current of the ith neuron [80]. Here, Δ_T is the slope factor and V_T is the spike-initiation threshold potential. Each neuron (say, the ith neuron) in the system is driven by an external stochastic feedforward input as $I_{i,\mathrm{ext}}=f\sum_l\delta(t-T_{i,l}^F)$. If the input current exceeds some threshold V_{th}, the membrane potential of the ith neuron V_i will diverge to infinity in finite time since $\psi_i(V)$ is supralinear. This divergence is identified as the emission of a spike of the ith neuron. And at the same time V_i is reset to the reset voltage V_R and is held at V_R for an absolute refractory period of τ_{ref} ms. Note that, with $V_{\mathrm{th}}=V_T$, the EI&F model reduces to the standard I&F model under the limit Δ_T goes to zero. Some parameters are chosen to be the same as those in I&F models and others in the reduced-dimensional units in the model (24) are chosen as [80,84]: $V_T=0.625$, $V_{\mathrm{th}}=4.375$, $V_R=-0.375$, $\Delta_T=0.4375$.

I&F networks with both excitation and inhibition

For a conductance-based I&F network with N_E excitatory neurons and N_I inhibitory neurons, its dynamics under Poisson drives is governed by

$$\begin{aligned}\frac{dV_{i,Q}}{dt} &= -G^L(V_{i,Q}-\epsilon^L)-G_{i,Q}^E(V_{i,Q}-\epsilon^E)-G_{i,Q}^I(V_{i,Q}-\epsilon^I),\\ \frac{dG_{i,Q}^E}{dt} &= -\frac{G_{i,Q}^E}{\sigma^E}+S_{QE}\sum_{j_E\neq i}^{N_E}\sum_k A_{ij_E}\delta(t-T_{j_E,k})+I_{i,\mathrm{ext}}^E,\\ \frac{dG_{i,Q}^I}{dt} &= -\frac{G_{i,Q}^I}{\sigma^I}+S_{QI}\sum_{j_I\neq i}^{N_I}\sum_k A_{ij_I}\delta(t-T_{j_I,k})+I_{i,\mathrm{ext}}^I,\end{aligned} \tag{25}$$

where the ith neuron with type $Q=E\,\mathrm{or}\,I$, has both excitatory conductance $G_{i,Q}^E$ and inhibitory conductance $G_{i,Q}^I$, and the ϵ^E and ϵ^I are the excitatory and inhibitory reversal potentials, respectively. If an excitatory neuron (say, the j_Eth neuron) fires and is presynaptic to the ith neuron (i.e., $A_{ij_E}=1$), the ith neuron's excitatory conductance $G_{i,Q}^E$ will be increased by the coupling strength S_{QE}. If an inhibitory neuron (say, the j_Ith neuron) fires and is presynaptic to the ith neuron (i.e., $A_{ij_I}=1$), the ith neuron's inhibitory conductance $G_{i,Q}^I$ will be increased by the coupling strength S_{QI}. [the corresponding physiological inhibitory postsynaptic potential (IPSP) is $\sim(30\times S_{QI}\,\mathrm{ms})\mathrm{mV}$]. The $I_{i,\mathrm{ext}}^{E}=f_E\sum_l\delta(t-T_{i,l}^{F,E})$ and $I_{i,\mathrm{ext}}^{I}=f_I\sum_l\delta(t-T_{i,l}^{F,I})$ are external Poisson drives for the ith neuron arising from background excitation and inhibition, respectively. For simplicity, we only consider the excitatory background input, i.e., $I_{i,\mathrm{ext}}^{I}=0$, and choose the input rate $\mu_E=\mu$ and input strength $f_E=f$. In the reduced-dimensional units, the parameters of inhibition in the model (25) are chosen as [117] $\epsilon^I=-2/3$, $\sigma^I=5$ ms, which correspond to typical physiological values, $\epsilon^I=-80$ mV. Other parameters are chosen to be the same as those in excitatory I&F models [Eq. (23)].

Supporting Information

Figure S1 GC from a subnetwork to a single neuron. For this nine-neuron network, we can divide it into one subnetwork and one single neuron, where the single neuron corresponds to neuron 7 and the subnetwork corresponds to the remaining eight neurons. Here, the subnetwork is presynaptic to the single neuron. Parameters are chosen as $\mu=1\ \mathrm{ms}^{-1}$ (Poisson input rate), $f=0.007\ \mathrm{ms}^{-1}$ (Poisson input strength), and the coupling strength $S=0.01\ \mathrm{ms}^{-1}$ (the corresponding EPSP is ~ 1 mV). (A) A nine-neuron network with its synaptic connectivity. (B) The constructed causal adjacency matrix $\mathrm{G}=(G_{ij})$ which captures the synaptic connectivity in (A). The white color in G_{ij} means there is no causal connection from neuron j to neuron i, i.e., $G_{ij}=0$, and the black color represents the existence of a causal connection from neuron j to neuron i, i.e., $G_{ij}=1$. (C) An effective two-neuron network constructed from (A), where the "neuron 1" represents the subnetwork that consists of all neurons in (A) except for neuron 7 as indicated by gray boxes (red online) in (B). The neuron 2 represents neuron 7 in (A). The voltage of "neuron 1" is the mean voltage averaged over all neurons in the subnetwork. (D) The computed causal adjacency matrix for (C), which successfully captures the unidirectional connection from the subnetwork "neuron 1" to the single neuron labeled by 2 [neuron 7 in (A)].
(EPS)

Figure S2 GC from a single neuron to a subnetwork. For this nine-neuron network, we can divide it into one subnetwork and one single neuron, where the single neuron corresponds to neuron 4 and the subnetwork corresponds to the remaining eight neurons. Here, the subnetwork is postsynaptic to the single neuron. Parameters are chosen as $\mu=1\ \mathrm{ms}^{-1}$ (Poisson input rate), $f=0.007\ \mathrm{ms}^{-1}$ (Poisson input strength), and the coupling strength $S=0.01\ \mathrm{ms}^{-1}$ (corresponding to EPSP ~ 1 mV). (A) A nine-neuron network with its synaptic connectivity. (B) The constructed causal adjacency matrix $\boldsymbol{G}=(G_{ij})$ which captures the synaptic connectivity in (A). The white color in G_{ij} means there is no causal connection from neuron j to neuron i, i.e., $G_{ij}=0$, and the black color represents the existence of causal connection from neuron j to neuron i, i.e., $G_{ij}=1$. (C) An effective two-neuron network constructed from (A), where neuron 1 represents neuron 4 in (A), "neuron 2" represents the entire network (A) except for neuron 4. The voltage of "neuron 2" is the voltage averaged over all neurons in the subnetwork, as indicated by gray boxes (red online). (D) The computed causal adjacency matrix for (C), which captures the unidirectional causal influence from the single neuron, labeled by 1 [neuron 4 in (A)], to the subnetwork "neuron 2".
(EPS)

Figure S3 GC between subnetworks. To construct subnetworks, we divide this fifteen-neuron network into three subnetworks and construct an effective three-"neuron" network. Parameters are chosen as $\mu=1\ \mathrm{ms}^{-1}$ (Poisson input rate), $f=0.007\ \mathrm{ms}^{-1}$ (Poisson input strength), and the coupling strength $S=0.01\ \mathrm{ms}^{-1}$ (corresponding to EPSP ~ 1 mV). (A) The synaptic adjacency matrix $\boldsymbol{A}=(A_{ij})$ for a fifteen-neuron network. The white color in A_{ij} indicates that there is no synaptic connection from neuron j to neuron i, i.e., $A_{ij}=0$ and the black color represents that the neuron j is presynaptic to the neuron i, i.e., $A_{ij}=1$. (B) The causal adjacency matrix $\boldsymbol{G}=(G_{ij})$ constructed by GC, which is identical to $\boldsymbol{A}$. (C) An effective three-neuron network constructed from (A), where the voltage of neuron "1","2" and "3" are the averaged response over each group of neurons, respectively. "Neuron 1" [indicated by the red box in (A)] represents a subnetwork from neuron 1 to neuron 5, "neuron 2" [indicated by the blue box in (A)] represents a subnetwork from neuron 6 to neuron 10, and "neuron 3" [indicated by the green box in (A)] represents a subnetwork from neuron 11 to neuron 15. (D) The computed causal adjacency matrix for (C), which captures the effective synaptic connections between the subnetworks.
(EPS)

Figure S4 GC connectivity using spike train. Network reconstruction by GC using the spike train time series of the I&F model. (A) The coincidence between the synaptic adjacency matrix $\boldsymbol{A}=(A_{ij})$ and the causal adjacency matrix $\boldsymbol{G}=(G_{ij})$ for the two-neuron network in Fig. 1A. The white color indicates that $\boldsymbol{A}\neq\boldsymbol{G}$, and the black color for $\boldsymbol{A}=\boldsymbol{G}$. (B) The absolute difference between $\boldsymbol{A}$ and $\boldsymbol{G}$, i.e., $|A_{ij}-G_{ij}|$, for the hundred-neuron network in Fig. 3A. The white color indicates that $|A_{ij}-G_{ij}|=1$, namely, $A_{ij}\neq G_{ij}$ and the black color for $A_{ij}=G_{ij}$. The total number of $A_{ij}\neq G_{ij}$ is 34 out of $\sim 10{,}000$ possible pairs of connections (with $p=0.001$ in the significance test). (C) Ranked GC in order of magnitude for the hundred-neuron network in Fig. 3A. The gray line (blue online) indicates a threshold in the gap of the ranked GC. Parameters are chosen as $\mu=0.24\ \mathrm{ms}^{-1}$ (Poisson input rate), $f=0.02\ \mathrm{ms}^{-1}$ (Poisson input strength), and the coupling strength $S=0.005\ \mathrm{ms}^{-1}$ (corresponding to EPSP ~ 0.5 mV).
(EPS)

Figure S5 GC analysis using spike train. Illustrated here is the validity of the relations used in the mechanism analysis computed by using the spike trains of the two excitatory neurons of the I&F network in Fig. 1A with different Poisson input rate μ for the highly fluctuating regime [(A) and (D)] with $\mu\sim 0.3\mathrm{ms}^{-1}$, intermediate regime [(B) and (E)] with $\mu\sim 0.8\mathrm{ms}^{-1}$ and mean-driven regime [(C) and (F)] with $\mu\sim 2.0\mathrm{ms}^{-1}$. The fixed input strength $f\sim 0.02\ \mathrm{ms}^{-1}$. (A), (B), and (C) are regression coefficients $\hat{b}_k^{\mathrm{J}}$ (blue "plus" online), $\hat{c}_k^{\mathrm{J}}$ (red "cross" online) and their approximations $Y_k=r_k/\mathrm{Var}(\epsilon_2^{\mathrm{A}})$ ("square" symbol), $Z_k=r_{-k}/\mathrm{Var}(\epsilon_1^{\mathrm{A}})$ ("circle" symbol) for three different dynamical regimes. (D), (E), and (F) are the GC $F_{S_1\rightarrow S_2}$ (red "star" online) as a function of coupling strength S for three different dynamical regimes. The line (black online) is a quadratic fit.
(EPS)

Figure S6 GC connectivity for EI&F networks. Network reconstruction by GC using the voltage time series of the EI&F model. (A) The coincidence between the synaptic adjacency matrix $\boldsymbol{A}=(A_{ij})$ and the causal adjacency matrix $\boldsymbol{G}=(G_{ij})$ for the two-neuron network in Fig. 1A. The white color indicates that $\boldsymbol{A}\neq\boldsymbol{G}$, and the black color for $\boldsymbol{A}=\boldsymbol{G}$. (B) The absolute difference between $\boldsymbol{A}$ and $\boldsymbol{G}$, i.e., $|A_{ij}-G_{ij}|$, for the hundred-neuron network in Fig. 3A. The white color indicates that $|A_{ij}-G_{ij}|=1$, namely, $A_{ij}\neq G_{ij}$ and the black color for $A_{ij}=G_{ij}$. The total number of $A_{ij}\neq G_{ij}$ is 68 out of $\sim 10{,}000$ possible pairs of connections (with

$p = 0.001$ in the significance test). The average neuronal firing rate is ~ 30 Hz. (C) Ranked GC in order of magnitude for the hundred-neuron network in Fig. 3A. The gray line (blue online) indicates a threshold in the gap of the ranked GC. Parameters are chosen as $\mu = 0.24\ \mathrm{ms}^{-1}$ (Poisson input rate), $f = 0.02\ \mathrm{ms}^{-1}$ (Poisson input strength), and the coupling strength $S = 0.005\ \mathrm{ms}^{-1}$ (corresponding to EPSP ~ 0.5 mV).
(EPS)

Figure S7 GC analysis for EI&F networks. Illustrated here is the validity of the relations in the mechanism analysis of GC computed by using the voltage time series of the two excitatory neurons of the EI&F network in Fig. 1A with different Poisson input rate μ for the highly fluctuating regime [(A) and (D)] with $\mu \sim 0.3\mathrm{ms}^{-1}$, intermediate regime [(B) and (E)] with $\mu \sim 0.8\mathrm{ms}^{-1}$ and low fluctuating regime [(C) and (F)] with $\mu \sim 2.0\mathrm{ms}^{-1}$. The fixed input strength $f \sim 0.02\ \mathrm{ms}^{-1}$. (A), (B), and (C) are regression coefficients $\hat{b}_k^{\mathrm{J}}$ (blue "plus" online), $\hat{c}_k^{\mathrm{J}}$ (red "cross" online) and their approximations $Y_k = r_k/\mathrm{Var}(\epsilon_2^{\mathrm{A}})$ ("square" symbol), $Z_k = r_{-k}/\mathrm{Var}(\epsilon_1^{\mathrm{A}})$ ("circle" symbol) for three different dynamical regimes. (D), (E), and (F) are the GC $F_{V_1 \to V_2}$ (red "star" online) for three different dynamical regimes. The line (black online) is a quadratic fit.
(EPS)

Figure S8 Minimal data length vs. neuronal firing rate. Illustrated here is the minimum data length required for GC reconstruction of the I&F network in Fig. 1A as a function of neuronal firing rate. (A) GC reconstruction using voltage time series with firing rate between 1Hz and 120Hz. (B) the same as (A) but using spike train time series. (C) the same as (A) but with firing rate between 0.08Hz and 1Hz. (D) the same as (B) but with firing rate between 0.08Hz and 1Hz. The Poisson input strength f is chosen as $f = 0.005\ \mathrm{ms}^{-1}$ [red "star", the line is for guiding the eye only.], $f = 0.01\ \mathrm{ms}^{-1}$ [blue "circle", the line is for guiding the eye only.] and the coupling strength $S = 0.01\ \mathrm{ms}^{-1}$ (corresponding to EPSP ~ 1 mV). The Poisson input rate μ is chosen to satisfy the corresponding neuronal firing rate.
(EPS)

Figure S9 GC ratio vs. the percentage of common Poisson input. Illustrated here are the GC ratios $F_{V_1 \to V_2}/F_{V_2 \to V_1}$ and $F_{S_1 \to S_2}/F_{S_2 \to S_1}$ for the I&F network in Fig. 1A. Neuron 1 and neuron 2 are driven by two independent background Poisson inputs with same rate μ and same strength f. In addition, both neurons are also driven by another common Poisson input (independent of their background Poisson input) with rate μ_0 and strength f. The percentage of common Poisson input P_{common} is defined by $\mu_0/(\mu + \mu_0)$. (A) The ratio of computed GC by using voltage time series: $F_{V_1 \to V_2}/F_{V_2 \to V_1}$ as a function of P_{common}. (B) The ratio of computed GC by using spike train time series: $F_{S_1 \to S_2}/F_{S_2 \to S_1}$ as a function of P_{common}. In (A) and (B), the red "star" symbol linked by solid line corresponds to the highly fluctuating regime with $\mu \sim 0.3\mathrm{ms}^{-1}$ as shown in Fig. 2A, the blue "circle" symbol linked by solid line corresponds to the intermediate regime with $\mu \sim 0.8\mathrm{ms}^{-1}$ as shown in Fig. 2B and the black "square" symbol linked by solid line corresponds to the mean-driven regime with $\mu \sim 2.0\mathrm{ms}^{-1}$ as shown in Fig. 2C. Parameters in (A) and (B) are chosen as $f = 0.02\ \mathrm{ms}^{-1}$ [red "star", the line is for guiding the eye only.], $f = 0.01\ \mathrm{ms}^{-1}$ [blue "circle", the line is for guiding the eye only.], $f = 0.005\ \mathrm{ms}^{-1}$ [black "square", the line is for guiding the eye only.] and the coupling strength $S = 0.01\ \mathrm{ms}^{-1}$ (corresponding to EPSP ~ 1 mV).
(EPS)

Text S1 Computational issues of GC.
(PDF)

Author Contributions

Conceived and designed the experiments: DZ YX YZ ZX DC. Performed the experiments: DZ YX YZ ZX DC. Analyzed the data: DZ YX YZ ZX DC. Contributed reagents/materials/analysis tools: DZ YX YZ ZX DC. Wrote the paper: DZ YX YZ ZX DC.

References

1. Newman MEJ (2003) The structure and function of complex networks. SIAM Review 45: 167–256.
2. Sporns O, Chialvo DR, Kaiser M, Hilgetag C (2004) Organization, development and function of complex brain networks. TRENDS in Cognitive Sciences 8: 418–425.
3. Honey CJ, Thivierge J, Sporns O (2010) Can structure predict function in the human brain? NeuroImage 52: 766–776.
4. Strogatz SH (2001) Exploring complex networks. Nature 410: 268–276.
5. Boccaletti S, Latora V, Moreno Y, Chavez M, Hwang DU (2006) Complex networks: structure and dynamics. Physics Reports 424: 175–308.
6. Bullmore E, Sporns O (2009) Complex brain networks: graph theoretical analysis of structural and functional systems. Nature Reviews Neuroscience 10: 186–198.
7. Jin X, Prince DA, Huguenard JR (2006) Enhanced excitatory synaptic connectivity in layer v pyramidal neurons of chronically injured epileptogenic neocortex in rats. The Journal of Neuroscience 26: 4891–4900.
8. Avramescu S, Timofeev I (2008) Synaptic strength modulation after cortical trauma: a role in epileptogenesis. The Journal of Neuroscience 28: 6760–6772.
9. Stetter O, Battaglia D, Soriano J, Geisel T (2012)Model-free reconstruction of excitatory neuronal connectivity from calcium imaging signals. PLoS Computational Biology 8: e1002653.
10. McIntosh AR, Gonzalez-Lima F (1994) Structural equation modeling and its application to network analysis in functional brain imaging. Human Brain Mapping 2: 2–22.
11. Buchel C, Friston KJ (1997) Modulation of connectivity in visual pathways by attention: cortical interactions evaluated with structural equation modelling and fmri. Cerebral Cortex 7: 768–778.
12. Schreiber T (2000) Measuring information transfer. Physical Review Letters 85: 461–464.
13. Gourevitch B, Eggermont J (2007) Evaluating information transfer between auditory cortical neurons. Journal of Neurophysiology 97: 2533–2543.
14. Ding M, Chen Y, Bressler SL (2006) Granger causality: basic theory and application to neuroscience. In Handbook of time series analysis, Schelter S, Winterhalder M, Timmer J, (eds) Wiley-VCH: Berlin: 437–460.
15. Guo S, Wu J, Ding M, Feng J (2008) Uncovering interactions in the frequency domain. PLoS Computational Biology 4: e1000087.
16. Ge T, Kendrick KM, Feng J (2009) A novel extended granger causal model approach demonstrates brain hemispheric differences during face recognition learning. PLoS Computational Biology 5: e1000570.
17. Lee L, Friston K, Horwitz B (2006) Large-scale neural models and dynamic causal modelling. NeuroImage 30: 1243–1254.
18. Neapolitan RE (2009) Probabilistic methods for bioinformatics: with an introduction to Bayesian networks. Morgan Kaufmann Publishers.
19. Friston K (1994) Functional and effective connectivity in neuroimaging: a synthesis. Human Brain Mapping 2: 56–78.
20. Horwitz B (2003) The elusive concept of brain connectivity. NeuroImage 19: 466–470.
21. Rubinov M, Sporns O (2010) Complex network measures of brain connectivity: uses and interpretations. NeuroImage 52: 1059–1069.
22. Honey CJ, Kotter R, Breakspear M, Sporns O (2007) Network structure of cerebral cortex shapes functional connectivity on multiple time scales. Proceedings of National Academy of Sciences of the United States of America 104: 10240–10245.
23. Honey CJ, Sporns O, Cammoun L, Gigandet X, Thiran JP, et al. (2009) Predicting human restingstate functional connectivity from structural connectivity. Proceedings of National Academy of Sciences of the United States of America 106: 2035–2040.
24. Zhou D, Xiao Y, Zhang Y, Xu Z, Cai D (2013) Causal and structural connectivity of pulse-coupled nonlinear networks. Physical Review Letters 111: 054102.
25. Gerhard F, Kispersky T, Gutierrez GJ, Marder E, Kramer M, et al. (2013) Successful reconstruction of a physiological circuit with known connectivity from spiking activity alone. PLoS Computational Biology 9: e1003138.

26. Hagmann P, Cammoun L, Gigandet X, Meuli R, Honey CJ, et al. (2008) Mapping the structural core of human cerebral cortex. PLoS Biology 6: 1479–1493.
27. Greicius MD, Supekar K, Menon V, Dougherty RF (2009) Resting-state functional connectivity reflects structural connectivity in the default mode network. Cerebral Cortex 19: 72–78.
28. Wang XJ (2010) Neurophysiological and computational principles of cortical rhythms in cognition. Physiological Review 90: 1195–1268.
29. Lehnertz K (2011) Assessing directed interactions from neurophysiological signals–an overview. Physiological Measurement 32: 1715–1724.
30. Carandini M, Mechler F, Leonard CS, Movshon JA (1996) Spike train encoding by regular-spiking cells of the visual cortex. Journal of Neurophysiology 76: 3425–3441.
31. Rauch A, Camera GL, Luscher H, Senn W, Fusi S (2003) Neocortical pyramidal cells respond as integrate-and-fire neurons to in vivo-like input currents. Journal of Neurophysiology 90: 1598–1612.
32. Burkitt AN (2006) A review of the integrate-and-fire neuron model: I. homogeneous synaptic input. Biological Cybernetics 95: 1–19.
33. Burkitt AN (2006) A review of the integrate-and-fire neuron model: Ii. inhomogeneous synaptic input and network properties. Biological Cybernetics 95: 97–112.
34. Tuckwell H (1988) Introduction to theoretical neurobiology. New York: Cambridge University Press.
35. Gerstner W, Kistler WM (2002) Spiking neuron models: Single neurons, populations, plasticity. Cambridge: Cambridge University Press.
36. Somers DC, Nelson SB, Sur M (1995) An emergent model of orientation selectivity in cat visual cortical simple cells. Journal of Neuroscience 15: 5448–5465.
37. Troyer TW, Krukowski AE, Priebe NJ, Miller KD (1998) Contrast-invariant orientation tuning in cat visual cortex: Thalamocortical input tuning and correlation-based intracortical connectivity. Journal of Neuroscience 18: 5908–5927.
38. Tao L, Shelley M, McLaughlin DW, Shapley R (2004) An egalitarian network model for the emergence of simple and complex cells in visual cortex. Proceedings of National Academy of Sciences of the United States of America 101: 366–371.
39. Cai D, Rangan AV, McLaughlin DW (2005) Architectural and synaptic mechanisms underlying coherent spontaneous activity in v1. Proceedings of National Academy of Sciences of the United States of America 102: 5868–5873.
40. Rangan AV, Cai D, McLaughlin DW (2005) Modeling the spatiotemporal cortical activity associated with the line-motion illusion in primary visual cortex. Proceedings of National Academy of Sciences of the United States of America 102: 18793–18800.
41. Rangan AV, Cai D (2007) Fast numerical methods for simulating large-scale integrate-and-fire neuronal networks. Journal of Computational Neuroscience 22: 81–100.
42. Zhou D, Rangan AV, Mclaughlin DW, Cai D (2013) Spatiotemporal dynamics of neuronal population response in the primary visual cortex. Proceedings of National Academy of Sciences of the United States of America 110: 9517–9522.
43. Granger C (1969) Investigating causal relations by econometric models and crossspectral methods. Econometrica 37: 424–438.
44. Geweke J (1982) Measurement of linear dependence and feedback between multiple time series. Journal of the American Statistical Association 77: 304–313.
45. Geweke J (1984) Measures of conditional linear dependence and feedback between time series. Journal of the American Statistical Association 79: 907–915.
46. Bressler SL, Seth AK (2011)Wiener-granger causality: a well established methodology. NeuroImage 58: 323–329.
47. Barnett L, Barrett AB, Seth AK (2009) Granger causality and transfer entropy are equivalent for gaussian variables. Physical Review Letters 103: 238701.
48. Upadhyay J, Silver A, Knaus TA, Lindgren KA, Ducros M, et al. (2008) Effective and structural connectivity in the human auditory cortex. The Journal of Neuroscience 28: 3341–3349.
49. Damoiseaux JS, Greicius MD (2009) Greater than the sum of its parts: a review of studies combining structural connectivity and resting-state functional connectivity. Brain Struct Funct 213: 525–533.
50. Kispersky T, Gutierrez GJ, Marder E (2011) Functional connectivity in a rhythmic inhibitory circuit using granger causality. Neural Systems & Circuits 1: 9–23.
51. Battaglia D, Witt A, Wolf F, Geisel T (2012) Dynamic effective connectivity of inter-areal brain circuits. PLoS Computational Biology 8: e1002438.
52. Matsumura M, Chen D, Sawaguchi T, Kubota K, Fetz EE (1996) Synaptic interactions between primate precentral cortex neurons revealed by spike-triggered averaging of intracellular membrane potentials in vivo. The Journal of Neuroscience 16: 7757–7767.
53. Bhalla US (2008) How to record a million synaptic weights in a hippocampal slice. PLoS Computational Biology 4: e1000098.
54. Rabinovich MI, Varona P, Selverston AI, Abarbanel H (2006) Dynamical principles in neuroscience. Reviews of Modern Physics 78: 1213–1265.
55. Seth AK (2005) Causal connectivity of evolved neural networks during behavior. Network: Computation in Neural Systems 16: 35–54.
56. Seth AK (2008) Causal networks in simulated neural systems. Cognitive Neurodynamics 2: 49–64.
57. Dayan P, Abbott L (2001) Theoretical neuroscience. Cambridge: MIT Press.
58. Zhou D, Rangan AV, Sun Y, Cai D (2009) Network-induced chaos in integrate-and-fire neuronal ensembles. Physical Review E 80: 031918.
59. Sun Y, Zhou D, Rangan AV, Cai D (2009) Library-based numerical reduction of the hodgkinhuxley neuron for network simulation. Journal of Computational Neuroscience 27: 369–390.
60. Komatsu Y, Nakajima S, Toyama K, Fetz EE (1988) Intracortical connectivity revealed by spiketriggered averaging in slice preparations of cat visual cortex. Brain Research 442: 359–362.
61. de Boer F, Kuyper P (1968) Triggered correlation. IEEE Transactions on Biomedical Engineering 15: 169–179.
62. Bhalla US (2008) How to record a million synaptic weights in a hippocampal slice. PLoS Computational Biology 4: e1000098.
63. Pandit S, Wu S (1983) Time series and system analysis with applications. New York: Wiley.
64. McQuarrie A, Tai CL (1998) Regression and time series model selection. New Jersey: World Scientific.
65. Lewicki MS (1998) A review of methods for spike sorting: the detection and classification of neural action potentials. Network 9: R53–78.
66. Buzsaki G (2004) Large-scale recording of neuronal ensembles. Nature Neuroscience 7: 446–451.
67. Brown EN, Kass RE, Mitra PP (2004) Multiple neural spike train data analysis: state-of-the-art and future challenges. Nature Neuroscience 7: 456–461.
68. Perkel DH, Gerstein GL, Moore GP (1967) Neuronal spike trains and stochastic point processes. i. the single spike train. Biophysical Journal 7: 391–418.
69. Perkel DH, Gerstein GL, Moore GP (1967) Neuronal spike trains and stochastic point processes. ii. simultaneous spike trains. Biophysical Journal 7: 419–440.
70. Snyder D, Miller M (1991) Random point processes in time and space, 2nd ed. New York: Springer-Verlag.
71. Daley D, Vere-Jones D (2003) An Introduction to the Theory of Point Process, 2nd ed. New York: Springer-Verlag.
72. Dhamala M, Rangarajan G, Ding M (2008) Estimating granger causality from fourier and wavelet transforms of time series data. Physical Review Letters 100: 018701.
73. Dhamala M, Rangarajan G, Ding M (2008) Analyzing information flow in brain networks with nonparametric granger causality. NeuroImage 41: 354–362.
74. Nedungadi AG, Rangarajan G, Jain N, Ding M (2009) Analyzing multiple spike trains with nonparametric granger causality. Journal of Computational Neuroscience 27: 55–64.
75. Lungarella M, Sporns O (2006) Mapping information flow in sensorimotor networks. PLoS Computational Biology 2: e144.
76. Truccolo W, Eden UT, Fellows MR, Donoghue JP, Brown EN (2005) A point process framework for relating neural spiking activity to spiking history, neural ensemble, and extrinsic covariate effects. Journal of Neurophysiology 93: 1074–1089.
77. Okatan M, Wilson MA, Brown EN (2005) Analyzing functional connectivity using a network likelihood model of ensemble neural spiking activity. Neural Computation 17: 1927–1961.
78. Kim S, Putrino D, Ghosh S, Brown EN (2011) A granger causality measure for point process models of ensemble neural spiking activity. PLoS Computational Biology 7: e1001110.
79. Wang XJ, Buzsaki G (1996) Gamma oscillation by synaptic inhibition in a hippocampal interneuronal network model. Journal of Neuroscience 16: 6402–6413.
80. Fourcaud-Trocme N, Hansel D, van Vreeswijk C, Brunel N (2003) How spike generation mechanisms determine the neuronal response to fluctuating inputs. Journal of Neuroscience 23: 11628–11640.
81. Badel L, Lefort S, Berger TK, Petersen CCH, Gerstner W, et al. (2008) Extracting non-linear integrate-and-fire models from experimental data using dynamic iv curves. Biological Cybernetics 99: 361–370.
82. Zhang L, McBain CJ (1995) Potassium conductances underlying repolarization and afterhyperpolarization in rat ca1 hippocampal interneurones. Journal of Physiology 488: 661–672.
83. Nowak LG, Azouz R, Sanchez-vives MV, Gray CM, McCormick DA (2003) Electrophysiological classes of cat primary visual cortical neurons in vivo as revealed by quantitative analyses. Journal of Neurophysiology 89: 1541–1566.
84. Geisler C, Brunel N, Wang XJ (2005) Contributions of intrinsic membrane dynamics to fast network oscillations with irregular neuronal discharges. Journal of Neurophysiology 94: 4344–4361.
85. Brette R, Gerstner W (2005) Adaptive exponential integrate-and-fire model as an effective description of neuronal activity. Journal of Neurophysiology 94: 3637–3642.
86. Koch MA, Norris DG, Hund-Georgiadis M (2002) An investigation of functional and anatomical connectivity using magnetic resonance imaging. NeuroImage 16: 241–250.
87. Sato JR, Junior EA, Takahashi DY, Felix MdM, Brammer MJ, et al. (2006) A method to produce evolving functional connectivity maps during the course of an fmri experiment using wavelet based time-varying granger causality. NeuroImage 31: 187–196.

88. Hu S, Liang H (2012) Causality analysis of neural connectivity: New tool and limitations of spectral granger causality. Neurocomputing 76: 44–47.
89. Song S, Sjostrom PJ, Reigl M, Nelson S, Chklovskii DB (2005) Highly nonrandom features of synaptic connectivity in local cortical circuits. PLoS Biology 3: e68.
90. Jia X, Kohn A (2011) Gamma rhythms in the brain. PLoS Biology 9: e1001045.
91. Emilio S, Sejnowski TJ (2000) Impact of correlated synaptic input on output firing rate and variability in simple neuronal models. The Journal of Neuroscience 20: 6193–6209.
92. Moreno R, Rocha J, Renart A, Parga N (2002) Response of spiking neurons to correlated inputs. Physical Review Letters 89: 288101.
93. Brette R (2009) Generation of correlated spike trains. Neural computation 21: 188–215.
94. Gutig R, Aharonov R, Rotter S, Sompolinsky H (2003) Learning input correlations through nonlinear temporally asymmetric hebbian plasticity. The Journal of Neuroscience 23: 3697–3714.
95. Newhall K, Kovacic G, Kramer P, Cai D (2010) Cascade-induced synchrony in stochasticallydriven neuronal networks. Physical Review E 82: 041903.
96. Newhall K, Kovacic G, Kramer P, Zhou D, Rangan AV, et al. (2010) Dynamics of current-based, poisson driven, integrate-and-fire neuronal networks. Communications in Mathematical Sciences 8: 541–600.
97. Zhang J, Newhall KA, Zhou D, Rangan AV (2013) Distribution of correlated spiking events in a population-based approach for integrate-and-fire networks. Journal of Computational Neuroscience DOI: 10.1007/s10827-013-0472-6.
98. Zhang J, Zhou D, Cai D, Rangan AV (2013) A coarse-grained framework for spiking neuronal networks: between homogeneity and synchrony. Journal of Computational Nueroscience: accepted.
99. Yu D, Righero M, Kocarev L (2006) Estimating topology of networks. Physical Review Letters 97: 188701.
100. Timme M (2007) Revealing network connectivity from response dynamics. Physical Review Letters 98: 224101.
101. Napoletani D, Sauer T (2008) Reconstructing the topology of sparsely connected dynamical networks. Physical Review E 77: 026103.
102. Smirnov DA, Bezruchko B (2009) Detection of couplings in ensembles of stochastic oscillators. Physical Review E 79: 046204.
103. Ren J, Wang WX, Li B, Lai YC (2010) Noise bridges dynamical correlation and topology in coupled oscillator networks. Physical Review Letters 104: 058701.
104. Levnajic Z, Pikovsky A (2011) Network reconstruction from random phase resetting. Physical Review Letters 107: 034101.
105. Shandilya SG, Timme M (2011) Inferring network topology from complex dynamics. New Journal of Physics 13: 013004.
106. KimWS, Cui XM, Yoon CN, Ta HX, Han SK (2011) Estimating network link weights from inverse phase synchronization indices. Europhysics Letters 96: 20006.
107. Prignano L, Diaz-Guilera A (2012) Extracting topological features from dynamical measures in networks of kuramoto oscillators. Physical Review E 85: 036112.
108. Van Bussel F, Kriener B, Timme M (2011) Inferring synaptic connectivity from spatio-temporal spike patterns. Frontiers in Computational Neuroscience 5: doi: 10.3389/fncom.2011.00003.
109. Mirollo RE, Strogatz SH (1990) Synchronization of pulse-coupled biological oscillators. SIAM Journal on Applied Mathematics 50: 1645–1662.
110. Marinazzo D, Pellicoro M, Stramaglia S (2008) Kernel method for nonlinear granger causality. Physical Review Letters 100: 144103.
111. Marinazzo D, Pellicoro M, Stramaglia S (2008) Kernel-granger causality and the analysis of dynamical networks. Physical Review E 77: 056215.
112. Wiener N (1956) The theory of prediction. In: Beckenbach E, (Ed) Modern mathematics for engineers McGraw-Hill, New York.
113. Seth AK (2010) A matlab toolbox for granger causal connectivity analysis. Journal of Neuroscience Methods 186: 262–273.
114. Hodgkin AL, Huxley AF (1952) A quantitative description of membrane current and its application to conduction and excitation in nerve. Journal of Physiology 117: 500–544.
115. Sun Y, Zhou D, Rangan AV, Cai D (2010) Pseudo-lyapunov exponents and predictability of hodgkin-huxley neuronal network dynamics. Journal of Computational Neuroscience 28: 247–266.
116. Zhou D, Sun Y, Rangan AV, Cai D (2010) Spectrum of lyapunov exponents of non-smooth dynamical systems of integrate-and-fire type. Journal of Computational Neuroscience 28: 229–245.
117. McLaughlin DW, Shapley R, Shelley M, Wielaard DJ (2000) A neuronal network model of macaque primary visual cortex (v1): Orientation selectivity and dynamics in the input layer 4c alpha. Proceedings of National Academy of Sciences of the United States of America 97: 8087–8092.

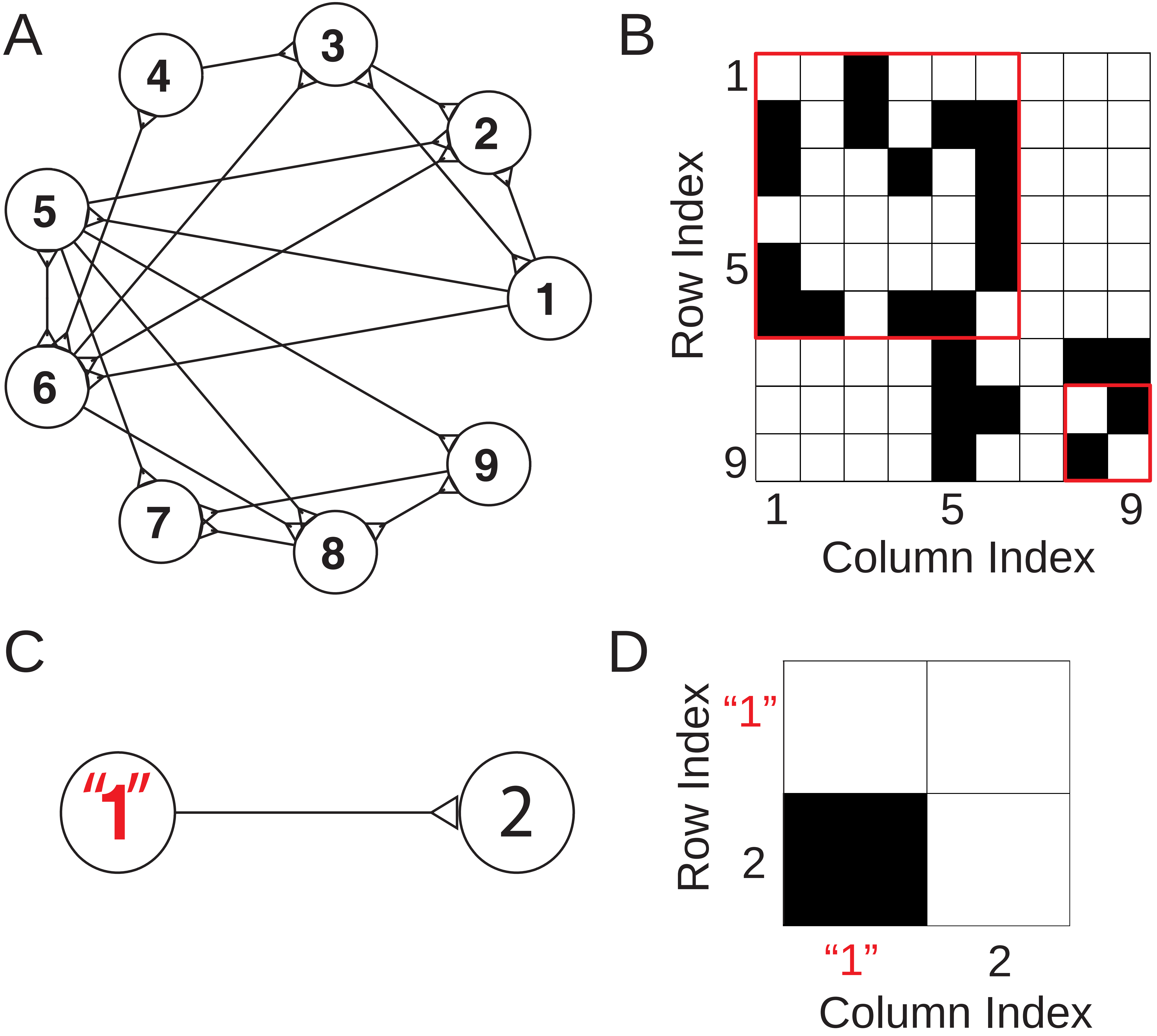
A
B
Row Index
Column Index
C
"1"
D
"1"
Row Index
"1"
Column Index

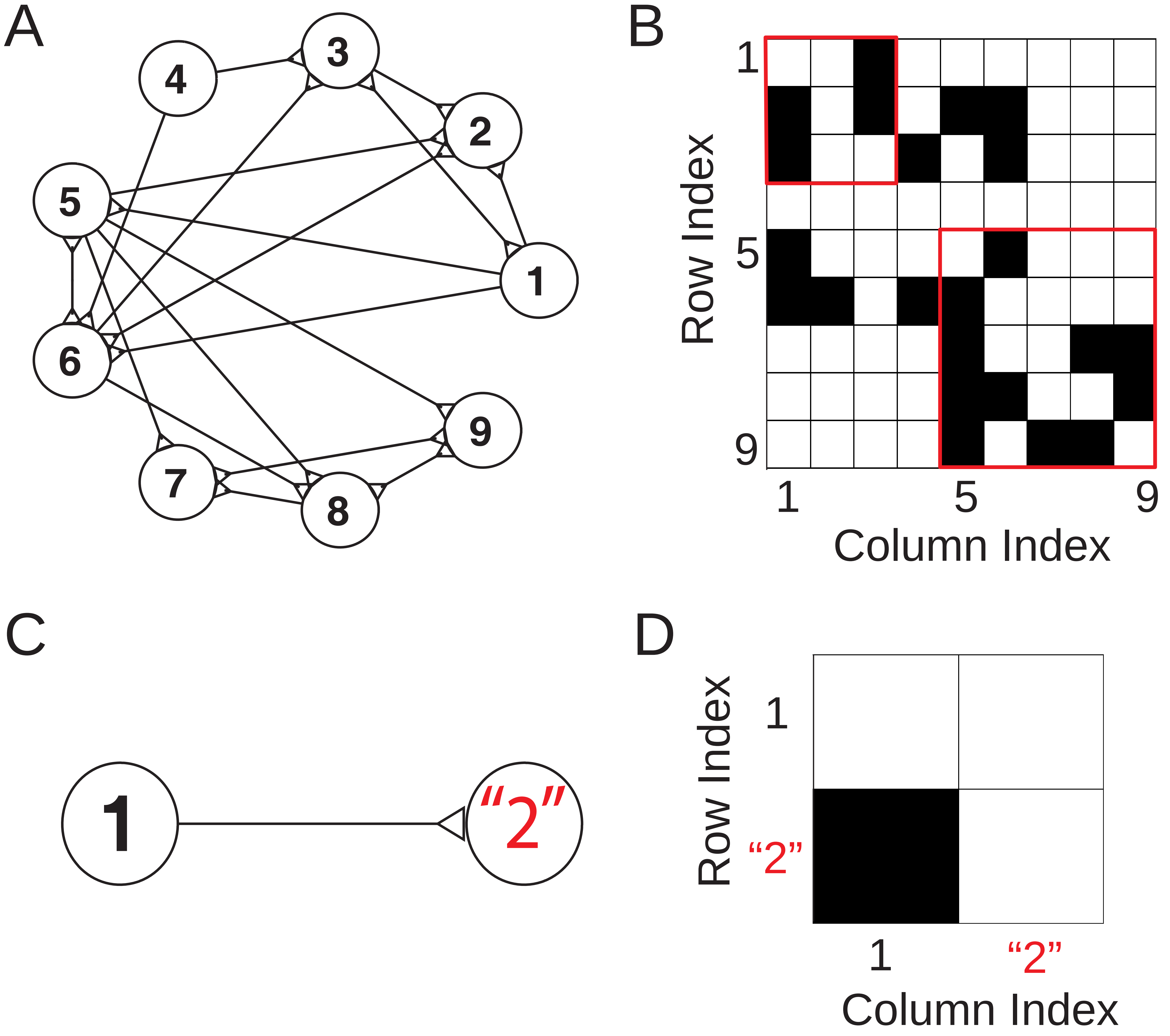
A
B
Row Index
Column Index
C
"2"
D
"2"
Row Index
"2"
Column Index

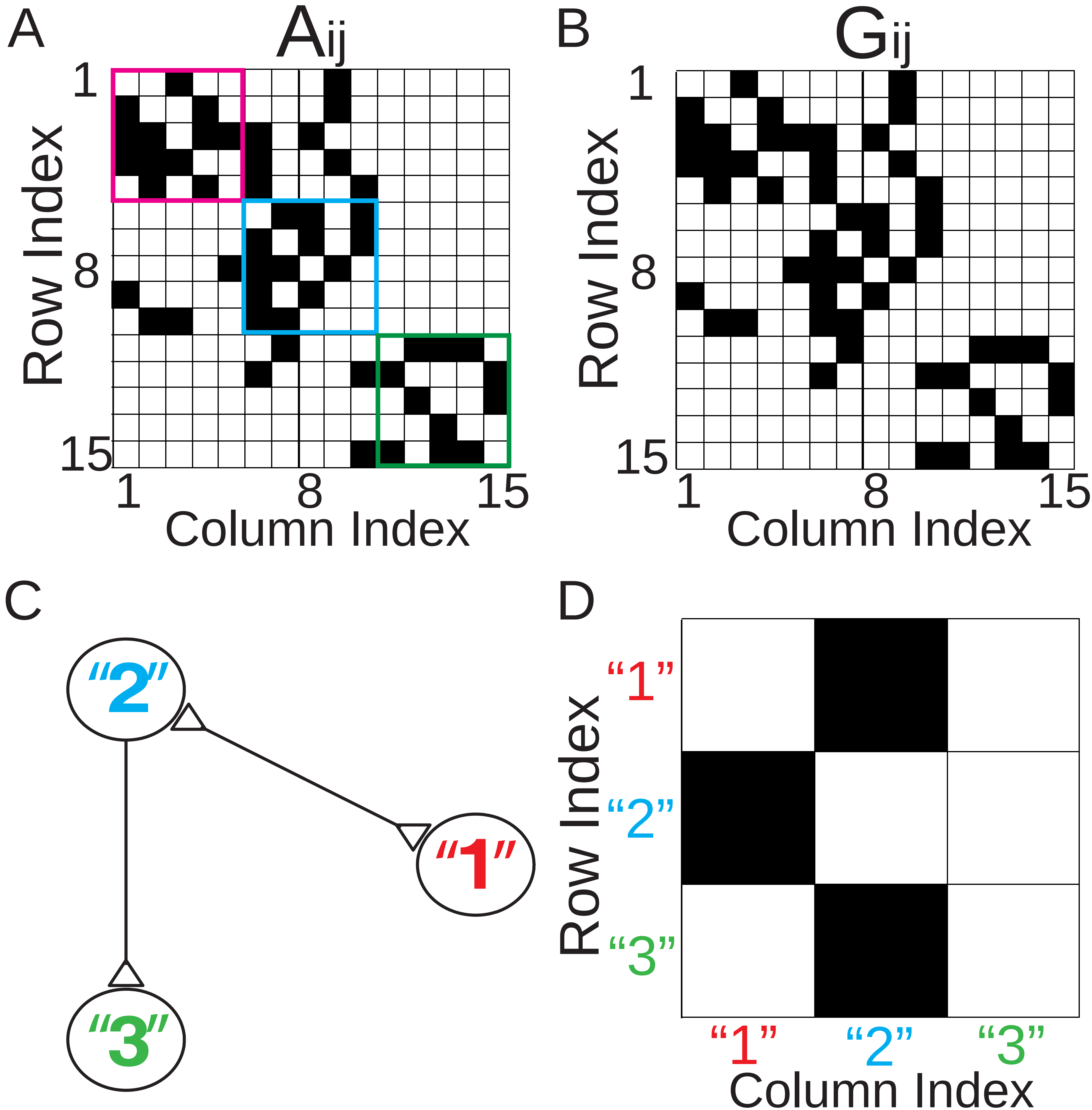
A
A_{ij}
Row Index
1
8
15
1
8
15
Column Index
B
G_{ij}
Row Index
1
8
15
1
8
15
Column Index
C
"2"
"1"
"3"
D
Row Index
"1"
"2"
"3"
"1"
"2"
"3"
Column Index

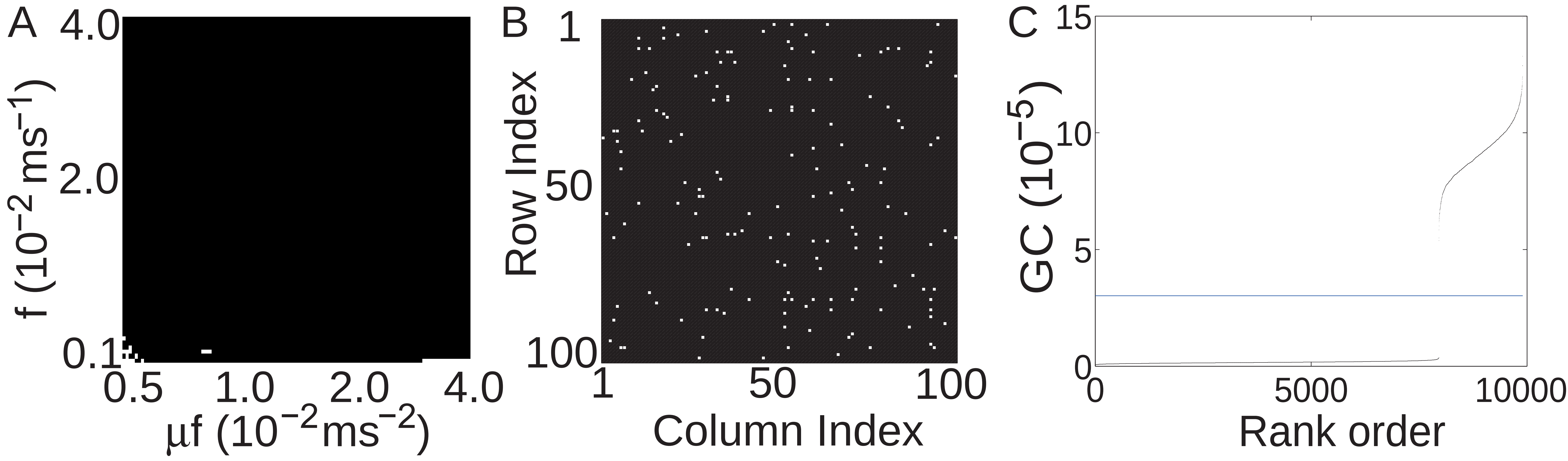
A
4.0
2.0
0.1
f (10^−2 ms^−1)
0.5
1.0
2.0
4.0
μf (10^−2 ms^−2)
B
1
50
100
Row Index
1
50
100
Column Index
C
15
10
5
0
GC (10^−5)
0
5000
10000
Rank order

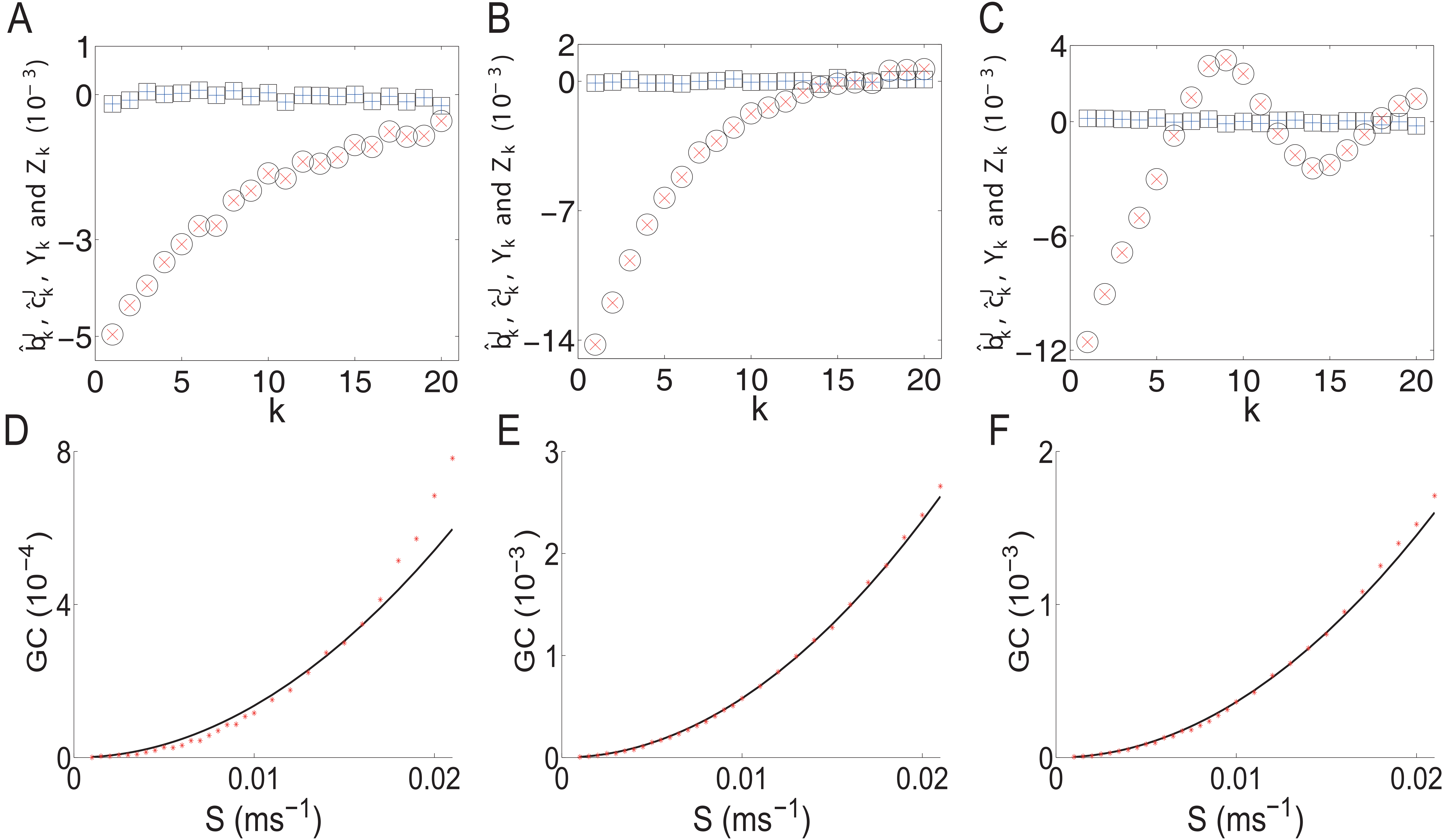
A
B
C
$\hat{b}^J_k$, $\hat{c}^J_k$, Y_k and Z_k (10^{-3})
1
0
−3
−5
2
0
−7
−14
4
0
−6
−12
0
5
10
15
20
k
D
E
F
GC (10^{-4})
GC (10^{-3})
8
4
0
3
2
1
0
2
1
0
0
0.01
0.02
S (ms^{-1})

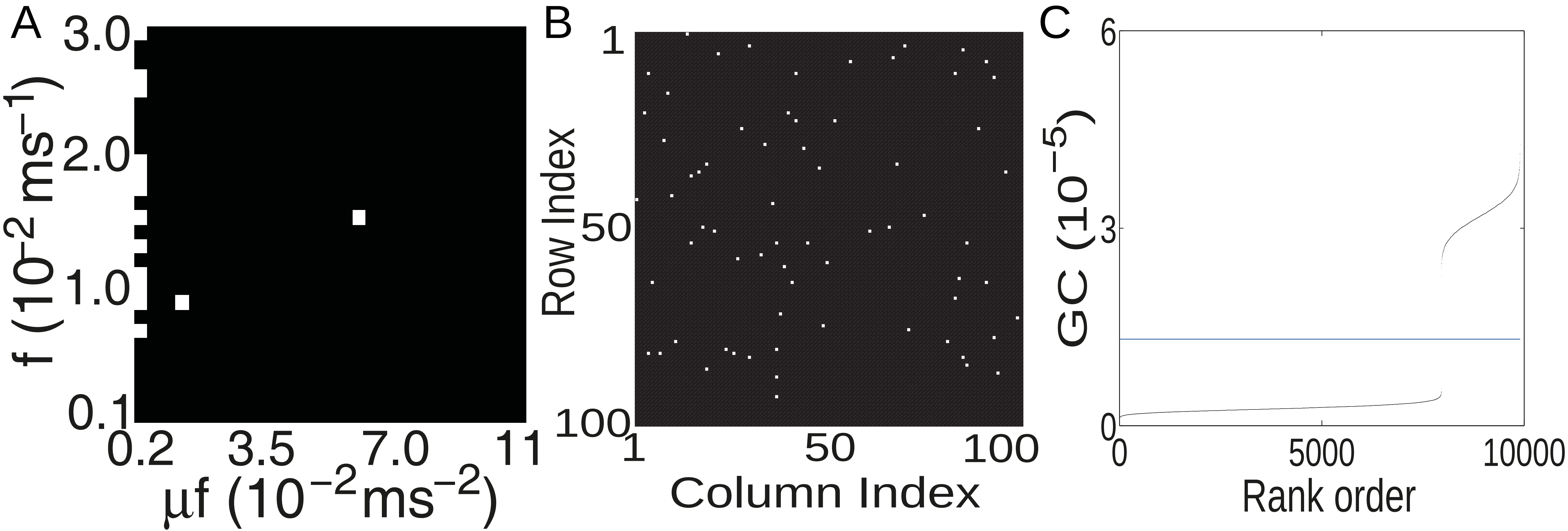
A
3.0
2.0
1.0
0.1
f $(10^{-2}\,\mathrm{ms}^{-1})$
0.2
3.5
7.0
11
μf $(10^{-2}\,\mathrm{ms}^{-2})$
B
1
50
100
Row Index
1
50
100
Column Index
C
6
3
0
GC (10^{-5})
0
5000
10000
Rank order

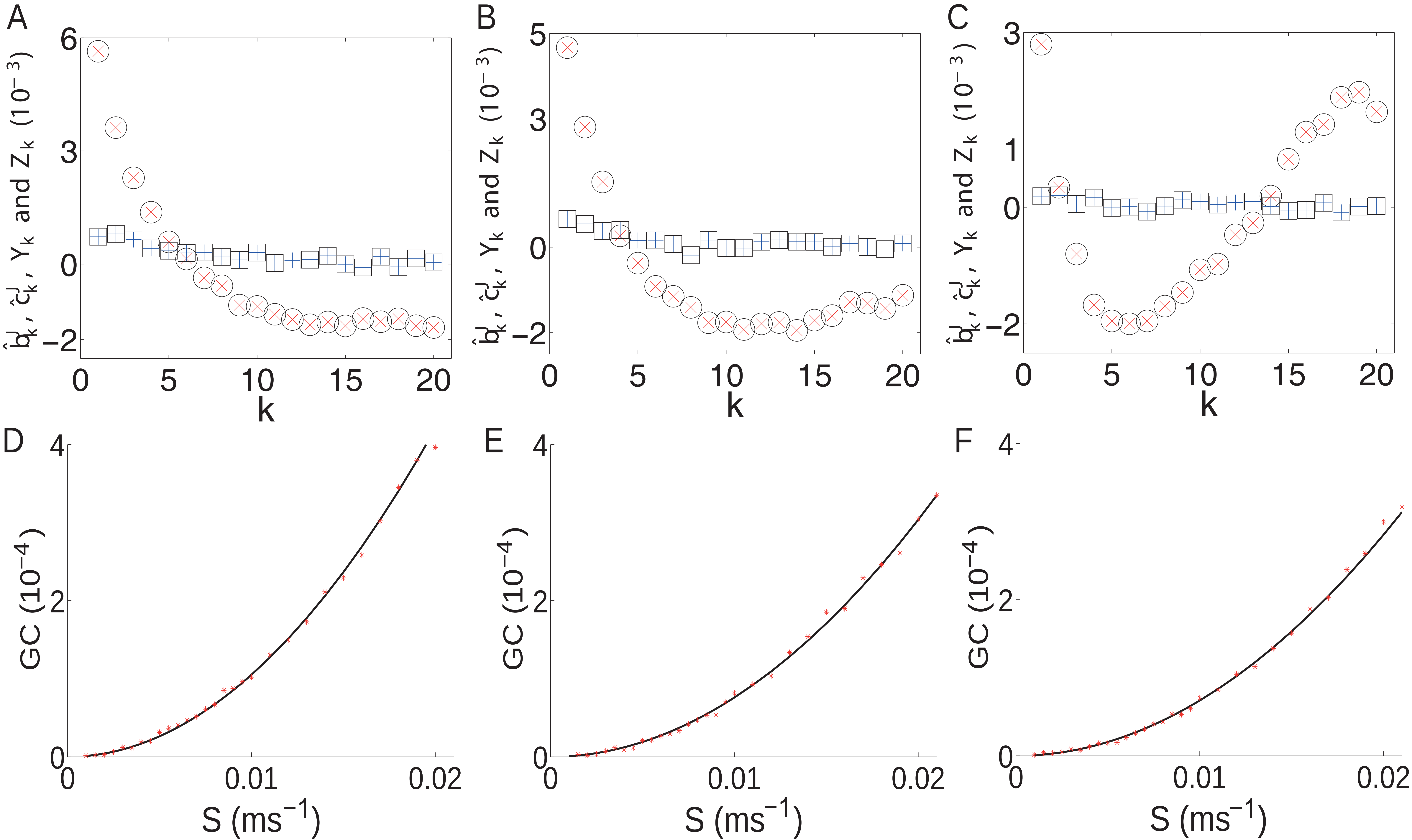
A
B
C
D
E
F
$\hat{b}^J_k$, $\hat{c}^J_k$, Y_k and Z_k (10^{-3})
k
0
5
10
15
20
6
3
0
−2
5
3
0
−2
3
1
0
−2
GC (10^{-4})
S (ms^{-1})
0
0.01
0.02
4
2
0

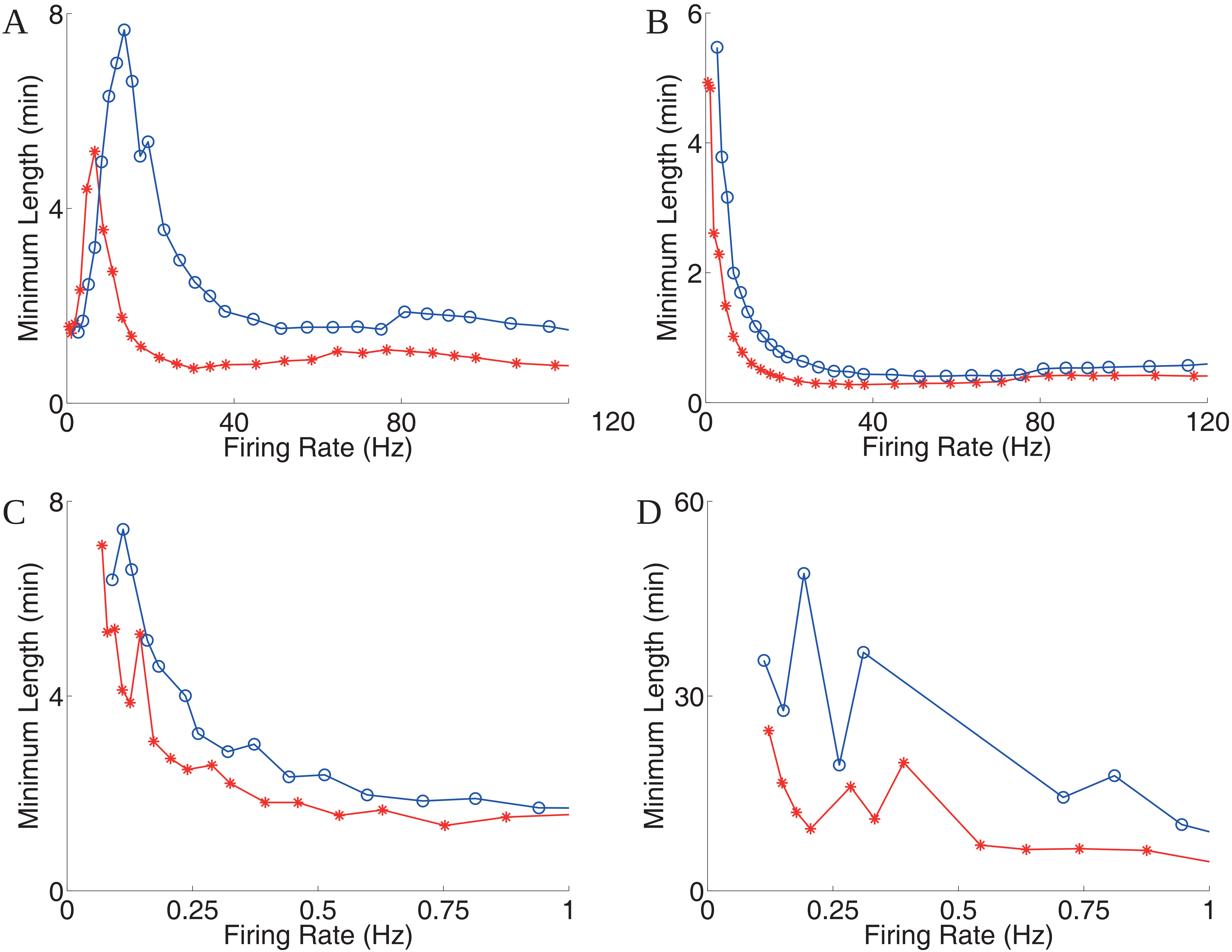
A
8
4
0
Minimum Length (min)
0
40
80
120
Firing Rate (Hz)
B
6
4
2
0
Minimum Length (min)
0
40
80
120
Firing Rate (Hz)
C
8
4
0
Minimum Length (min)
0
0.25
0.5
0.75
1
Firing Rate (Hz)
D
60
30
0
Minimum Length (min)
0
0.25
0.5
0.75
1
Firing Rate (Hz)

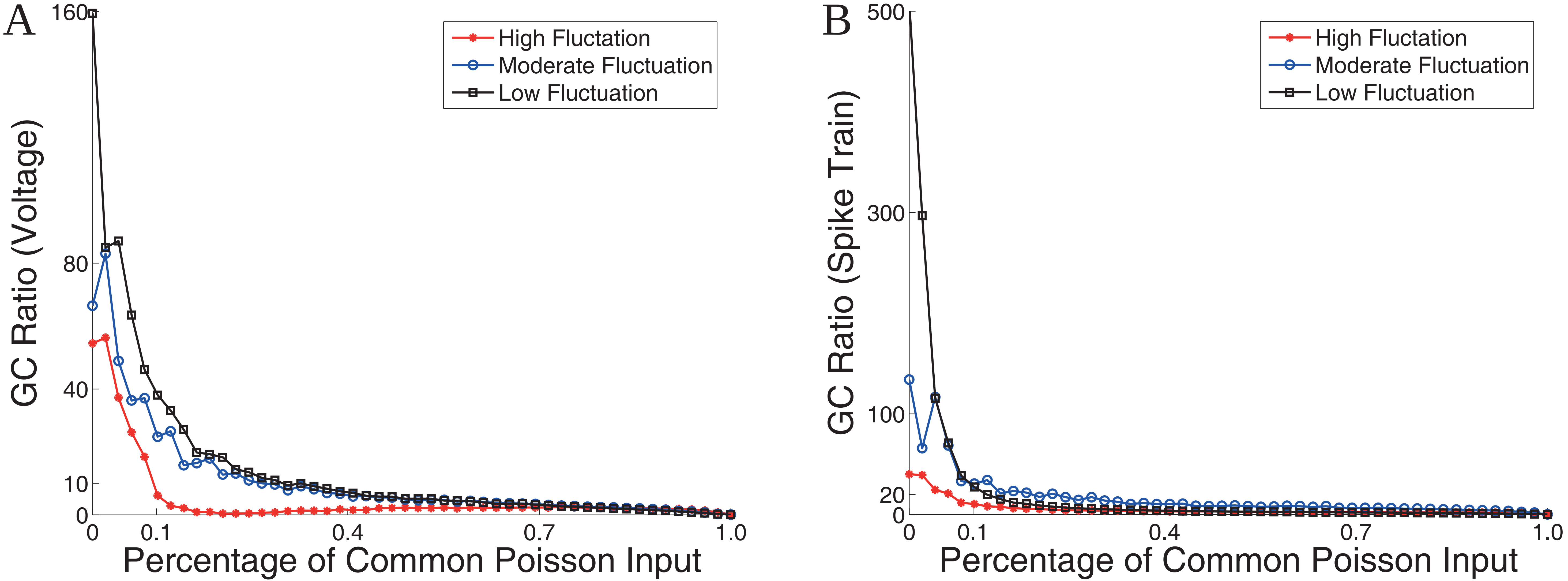
A
GC Ratio (Voltage)
160
80
40
10
0
0
0.1
0.4
0.7
1.0
Percentage of Common Poisson Input
High Fluctation
Moderate Fluctuation
Low Fluctuation
B
GC Ratio (Spike Train)
500
300
100
20
0
0
0.1
0.4
0.7
1.0
Percentage of Common Poisson Input
High Fluctation
Moderate Fluctuation
Low Fluctuation

Supporting Information

Granger Causality Network Reconstruction of Conductance-based Integrate-and-Fire Neuronal Systems

Douglas Zhou, Yanyang Xiao, Yaoyu Zhang, Zhiqin Xu, David Cai

Computational issues of GC

In the theoretical definition of GC, one assumes that the data length of time series and the regression order in autoregressive processes are both infinite [1]. In practice, however, the measured time series in experiment has only finite length. With finite-length data, some important issues have to be addressed. The first issue is how to choose a correct regression order since the total length of data is finite. It has been shown that an improper choice of regression order can cause large errors in linear regression models [2, 3]. The second issue is to determine whether the causal influence between time series is statistically significant or arises from statistical error introduced by finite-length data and finite regression orders in the numerical computation of GC.

In the following, we discuss the methodology to address the above issues along with the numerical algorithm of evaluating GC for a given set of empirical time series $\{x_i(t)\}_{i=1}^N$. Let $\boldsymbol{X}_t = [\hat{x}_1(t),\, \hat{x}_2(t),\, \cdots,\, \hat{x}_N(t)]^T$ be an N dimensional time series with L being the length for simultaneously recorded $\{x_i(t)\}_{i=1}^N$. Here, the notation of superscript T in $\boldsymbol{X}_t$ represents matrix transposition and $\hat{x}_i(t) = x_i(t) - \mathbb{E}[x_i(t)]$ has a zero mean. Assuming that $\boldsymbol{X}_t$ is stationary, for a given regression order $\hat{m}$, we can construct the following regressive equations [2, 3]

$$\boldsymbol{X}_t + \boldsymbol{A}_1\boldsymbol{X}_{t-1} + \cdots + \boldsymbol{A}_{\hat{m}}\boldsymbol{X}_{t-\hat{m}} = \boldsymbol{E}_{(\hat{m})}(t), \tag{1}$$

where $\boldsymbol{A}_i$ are $N \times N$ regression-coefficient matrices ($i = 1, 2, \cdots, \hat{m}$) and $\boldsymbol{E}_{(\hat{m})}(t) = [\epsilon_1^{(\hat{m})}(t),\, \epsilon_2^{(\hat{m})}(t),\, \cdots,\, \epsilon_N^{(\hat{m})}(t)]^T$ is a vector of residuals which have zero mean. The covariance matrix of $\boldsymbol{E}_{(\hat{m})}(t)$, denoted by $\boldsymbol{\Sigma}_{\hat{m}}$, is given by

$$\boldsymbol{\Sigma}_{\hat{m}} = \langle \boldsymbol{E}_{(\hat{m})}(t)\boldsymbol{E}_{(\hat{m})}^T(t)\rangle. \tag{2}$$

Note that the correlation between $\boldsymbol{E}_{(\hat{m})}(t)$ and $\boldsymbol{X}_{t-k}$ (for any $1 \le k \le \hat{m}$) is zero. Therefore, by multiplying $\boldsymbol{X}_{t-k}^T$ ($k = 1, 2, \cdots, \hat{m}$) on both sides of Eqs. (1) and then taking expectations, we can obtain the Yule-Walker equations as follows [2, 3]

$$\boldsymbol{C}_{-k} + \boldsymbol{A}_1\boldsymbol{C}_{-k+1} + \cdots + \boldsymbol{A}_{\hat{m}}\boldsymbol{C}_{-k+\hat{m}} = 0, \quad 1 \le k \le \hat{m}, \tag{3}$$

where $\boldsymbol{C}_\tau = \langle \boldsymbol{X}_t\boldsymbol{X}_{t+\tau}^T\rangle$ is the covariance matrix of $\boldsymbol{X}_t$ and $\boldsymbol{C}_{-\tau} = \boldsymbol{C}_\tau^T$ for $\tau \ge 0$.

To obtain the regression coefficients $\boldsymbol{A}_1,\ \boldsymbol{A}_2,\ \cdots,\ \boldsymbol{A}_{\hat{m}}$, we rewrite Eqs. (3) as

$$\begin{pmatrix} \boldsymbol{C}_0 & \boldsymbol{C}_1^T & \cdots & \boldsymbol{C}_{\hat{m}-1}^T \\ \boldsymbol{C}_1 & \boldsymbol{C}_0 & \cdots & \boldsymbol{C}_{\hat{m}-2}^T \\ \vdots & \vdots & \ddots & \vdots \\ \boldsymbol{C}_{\hat{m}-1} & \boldsymbol{C}_{\hat{m}-2} & \cdots & \boldsymbol{C}_0 \end{pmatrix} \begin{pmatrix} \boldsymbol{A}_1^T \\ \boldsymbol{A}_2^T \\ \vdots \\ \boldsymbol{A}_{\hat{m}}^T \end{pmatrix} = - \begin{pmatrix} \boldsymbol{C}_1 \\ \boldsymbol{C}_2 \\ \vdots \\ \boldsymbol{C}_{\hat{m}} \end{pmatrix} \tag{4}$$

For simplicity, we denote the symmetrical coefficient matrix of linear equations (4) by

$$\boldsymbol{\Omega}_{\hat{m}\times\hat{m}} = [\boldsymbol{\Omega}_{ij}]_{\hat{m}\times\hat{m}}, \quad \text{where} \quad \boldsymbol{\Omega}_{ij} = \boldsymbol{C}_{i-j}, \tag{5}$$

the regression coefficient matrices by

$$\Lambda_{\hat{m}} = [\boldsymbol{A}_1, \boldsymbol{A}_2, \cdots, \boldsymbol{A}_{\hat{m}}]^T, \tag{6}$$

and the right hand side of Eqs. (4) by

$$\boldsymbol{B}_{\hat{m}} = -[\boldsymbol{C}_1^T, \boldsymbol{C}_2^T, \cdots, \boldsymbol{C}_{\hat{m}}^T]^T. \tag{7}$$

Equations (4) then becomes $\boldsymbol{\Omega}_{\hat{m}\times\hat{m}}\Lambda_{\hat{m}} = \boldsymbol{B}_{\hat{m}}$. Note that (i) Eqs. (4) contain a total number of $\hat{m}N^2$ unknown regression coefficients in $\Lambda_{\hat{m}}$ and we have exactly the same number of linear equations; (ii) the coefficient matrix $\boldsymbol{\Omega}_{\hat{m}\times\hat{m}}$ in linear equations (4), in general, should be positive definite when the data length L is infinite.

Construction of positive definite matrix $\boldsymbol{\Omega}_{\hat{m}\times\hat{m}}$

As is well known, the properties of the coefficient matrix, e.g., symmetric and positive definiteness, play an important role in determining the robustness of numerical solutions to linear equations [4, 5]. Mathematically, the coefficient matrix $\boldsymbol{\Omega}_{\hat{m}\times\hat{m}}$ in Eqs. (4) is positive definite when the length of time series L is infinite. In numerical computations, however, if we first compute each covariance matrix function $\boldsymbol{C}_k,\ k = 0, 1, \cdots, \hat{m}-1$, and then construct the coefficient matrix $\boldsymbol{\Omega}_{\hat{m}\times\hat{m}}$ as in Eqs. (4) and (5), due to statistical effects caused by finite data length, $\boldsymbol{\Omega}_{\hat{m}\times\hat{m}}$ is not guaranteed to be positive definite. Therefore, when solving linear equations (4) to obtain the regression coefficients $\Lambda_{\hat{m}}$, one may obtain an incorrect inference of the causal connectivities between neurons.

To numerically construct $\boldsymbol{\Omega}_{\hat{m}\times\hat{m}}$ that preserves the property of positive definiteness, we define $\boldsymbol{Y}_t = [\boldsymbol{X}_{t+\hat{m}-1}^T,\ \boldsymbol{X}_{t+\hat{m}-2}^T,\ \cdots,\ \boldsymbol{X}_t^T]^T$, which is an $\hat{m}N$ dimensional vector. The coefficient matrix $\boldsymbol{\Omega}_{\hat{m}\times\hat{m}}$ can be obtained by

$$\boldsymbol{\Omega}_{\hat{m}\times\hat{m}} = \langle \boldsymbol{Y}_t \boldsymbol{Y}_t^T \rangle = \frac{1}{L-\hat{m}+1} \sum_{t=1}^{L-\hat{m}+1} \boldsymbol{Y}_t \boldsymbol{Y}_t^T. \tag{8}$$

In our cases, numerical simulations have shown that the coefficient matrix $\boldsymbol{\Omega}_{\hat{m}\times\hat{m}}$ as constructed in Eqs. (8) is always positive definite when the length of time series L is finite ($L > \hat{m}N$). After this, Eqs. (4) can be solved by many robust numerical algorithms such as the conjugate gradient method, Cholesky decomposition method or successive relaxation method [4, 5, 6].

Regression order

To obtain a good estimate of GC, it is important to determine a correct regression order m in linear regression models [7]. Some criteria have been proposed based on the information theory [8, 9]. One is the Akaike Information Criterion (AIC), which is defined by minimizing the AIC function with respect to $\hat{m}$. The AIC function is defined as

$$AIC(\hat{m}) = \ln[\det(\mathbf{\Sigma}_{\hat{m}})] + \frac{2\hat{m}N^2}{L}, \tag{9}$$

where $\det(\mathbf{\Sigma}_{\hat{m}})$ is the determinant of the covariance matrix $\mathbf{\Sigma}_{\hat{m}}$ as defined in Eqs. (2). The other criterion is the Bayesian Information Criterion (BIC) and the regression order $\hat{m}$ is chosen by minimizing the BIC function as

$$BIC(\hat{m}) = \ln[\det(\mathbf{\Sigma}_{\hat{m}})] + \frac{\hat{m}N^2 \ln L}{L}. \tag{10}$$

It has been shown that the AIC function sometimes cannot achieve a minimum when the total number of data points L is large. However, the BIC criterion can compensate for the large number of data points and usually performs better in neural applications [1]. In our study, both AIC and BIC criteria have been tested to determine the regression order $\hat{m}$, and $\hat{m}$ determined by the AIC criterion is usually larger than that obtained by using the BIC criterion. However, the final results about the inference of causal interactions between time series remain the same for both criteria.

Statistical significance

In numerical computations, due to finite data length L and finite regression order m, we can only obtain an estimate of GC, denoted by $\hat{F}$. Therefore, we should perform significance tests to determine whether the calculated nonzero $\hat{F}$ is statistically significant or it arises from statistical error. Under the null hypothesis that there is no causal influence from x_2 to x_1, the conventional large-sample distribution theory can be used [10, 2, 3] to show that $\hat{F}_{x_2\to x_1}$ is asymptotically χ^2 distributed as $L\hat{F}_{x_2\to x_1} \sim \chi^2(m)$. We can obtain a threshold for GC magnitude from x_2 to x_1 (similarly for the GC $\hat{F}_{x_1\to x_2}$) through a p-value test [11, 2, 3]. In most of our cases, p is chosen to be 0.001 in numerical simulations.

In addition, if we want to obtain the confidence interval for the theoretically defined but unknown GC, denoted by F [11, 12], The statistical significance can be similarly analyzed by using the χ^2 statistic, which is asymptotically monotonically related to the F-statistic [11, 13]. For ease of discussion, we consider the significance test for two time series $x_1(t)$ and $x_2(t)$. However, this test can be straightforwardly extended to the multivariate case.

Suppose $F_{x_1\to x_2}$ and $F_{x_2\to x_1}$ are the theoretical GC, whereas $\hat{F}_{x_1\to x_2}$ and

$\hat{F}_{x_2 \to x_1}$ are the estimate of GC from empirical time series, we have

$$\begin{aligned} L\hat{F}_{x_1 \to x_2} &\sim \chi'^2(m, LF_{x_1 \to x_2}), \\ L\hat{F}_{x_2 \to x_1} &\sim \chi'^2(m, LF_{x_2 \to x_1}), \end{aligned} \tag{11}$$

where $\chi'^2(n, \lambda)$ is a noncentral χ^2 distribution with mean λ and the degree of freedom n. In practice, a direct numerical evaluation of the noncentral χ^2 distribution is usually difficult. However, there are some good approximations [14, 15]. For instance, if $x \sim \chi'^2(n, \lambda)$, then

$$\sqrt{x - (n-1)/3} \sim N(\sqrt{\lambda + (2n+1)/3}, 1) \quad \text{for} \quad x \geq (n-1)/3.$$

Using these approximations, one can obtain an approximate 95 percent confidence interval for $F_{x_1 \to x_2}$ and $F_{x_2 \to x_1}$ as

$$\begin{aligned} \phi_l(\hat{F}_{x_1 \to x_2}, m, L) < &F_{x_1 \to x_2} < \phi_r(\hat{F}_{x_1 \to x_2}, m, L), \\ \phi_l(\hat{F}_{x_2 \to x_1}, m, L) < &F_{x_2 \to x_1} < \phi_r(\hat{F}_{x_2 \to x_1}, m, L), \end{aligned}$$

where the functions $\phi_l(\cdot)$ and $\phi_r(\cdot)$ are defined as

$$\begin{aligned} \phi_l(x, m, L) &= (\sqrt{x - \frac{m-1}{3L}} - \frac{1.96}{\sqrt{L}})^2 - \frac{2m+1}{3L}, \\ \phi_r(x, m, L) &= (\sqrt{x - \frac{m-1}{3L}} + \frac{1.96}{\sqrt{L}})^2 - \frac{2m+1}{3L}. \end{aligned}$$

Minimal data length for GC reconstruction

Here, we discuss the minimal data length that is needed for a successful GC reconstruction. As an illustration of this issue, we study the two-neuron network as shown in Fig. 1A. From the conventional large-sample distribution theory [2, 3, 10], the numerical computed GC values $\hat{F}_{x_1 \to x_2}$ and $\hat{F}_{x_2 \to x_1}$ are asymptotically χ^2 distributed as shown in Eq. (11) and we record their probability distribution function as $\rho_1(x)$ (with causal influence) and $\rho_0(x)$ (without causal influence), respectively. As discussed in the main text, we can determine a GC threshold F_{T} by performing the p-value test. Therefore, the probability of correct topology reconstruction for this network is

$$P[\text{correct}] = \int_0^{\mathrm{F_T}} \rho_0(\mathrm{x})\mathrm{dx} \int_{\mathrm{F_T}}^{+\infty} \rho_1(\mathrm{x})\mathrm{dx} \tag{12}$$

Note that, the distributions $\rho_1(x)$ and $\rho_0(x)$ depend on the theoretical GC values $F_{x_1 \to x_2}$ and $F_{x_2 \to x_1}$, respectively. As discussed above, $F_{x_1 \to x_2}$ and $F_{x_2 \to x_1}$ are theoretically defined using infinite length of time series. Therefore, we compute GC values by using sufficiently long time series (~ 200 mins) until our numerical results are convergent and can well approximate those theoretical GC values. For a given level of correctness $P[\text{correct}]$ (e.g., 90%), Eq. (12) is an implicit function of time length [See Eq. (11)] and we can solve it using an iterative method to obtain the minimal data length $L_{\min}$ for the GC reconstruction as shown in Fig. S8.

References

[1] Ding M, Chen Y, Bressler SL (2006) Granger causality: basic theory and application to neuroscience. In Handbook of time series analysis, Schelter S, Winterhalder M, Timmer J (eds) Wiley-VCH: Berlin : 437-460.

[2] Pandit S, Wu S (1983) Time series and system analysis with applications. New York: Wiley.

[3] McQuarrie A, Tai CL (1998) Regression and time series model selection. New Jersey: World Scientific.

[4] Meyer CD (2001) Matrix Analysis and Applied Linear Algebra. Society for Industrial and Applied Mathematics.

[5] Leon SJ (2006) Linear Algebra With Applications (7th ed.). Pearson Prentice Hall.

[6] Whaley RC, Petitet A, Dongarra JJ (2001) Automated empirical optimizations of software and the atlas project. Parallel Computing 27: 3-35.

[7] Schwartz G (1978) Estimating the dimension of a model. The Annals of Statistics 5: 461-464.

[8] Akaike H (1969) Fitting autoregressive models for prediction. Annals of the Institute of Statitical Mathematics 21: 243-247.

[9] Akaike H (1978) A bayesian analysis of the minimum aic procedure. Annals of the Institute of Statitical Mathematics 30: 9-14.

[10] Greene WH (2002) Econometric analysis, fifthe ed. New Jersy: Prentice-Hall.

[11] Geweke J (1982) Measurement of linear dependence and feedback between multiple time series. Journal of the American Statistical Association 77: 304-313.

[12] Geweke J (1984) Measures of conditional linear dependence and feedback between time series. Journal of the American Statistical Association 79: 907-915.

[13] Bressler SL, Seth AK (2011) Wiener-granger causality: a well established methodology. NeuroImage 58: 323-329.

[14] Sankaran M (1963) Approximations to the non-central chi-square distribution. Biometrika 50: 199-204.

[15] Johnson NL, Kotz S (1970) Distributions in statistics: continuous univariate distributions (Vol. 2). New York: John Wiley.